Master thesis
Study of the new DSSD for Belle SVD

Department of Physics, Tohoku University
Nobuhiro Tani

January, 2007

Abstract

There are many theories beyond the SM. One way to discover a new physics beyond SM is the high-luminosity collider experiment to measure the phenomena whose amplitude is quite small. The Belle experiment are conducted for this purpose.

In the Belle experiment, the CP violation through B meson decay is studied. Since it needs quite large data set, the luminosity of KEKB accelerator is developing in order to generate more B mesons. Thus, the innermost detector SVD, which is a key device for time dependent CP asymmetries, will be exposed to more beam background.

To cope with this problem, we plan to install SVD3 in 2007. The main improvement of this upgrade is to introduce APV25 readout chip with faster peaking time. However its faster peaking time degrades the performance of current DSSD because of larger noise from detector capacitance.

Then we prepare a prototype sensor with 5 configurations which are expected to perform well with APV25. I measure the capacitance between neighboring strips which is dominant component of detector capacitance, and it is almost same as expected.

To measure the performance of the prototype on the close condition to the real operation, we did a beam test by using 4GeV π^- beam. For all configurations, we confirm the good hit-finding efficiency ($\sim$99%), and enough S/N of the sensor (more than 20). The better spatial resolution is obtained when the sensor has wider P-stop gap structure. When P-stop gap is wide, the mean

value of cluster width becomes large because the charge from particles passing between two strips are well-shared to both strips, and this results in the good spatial resolution.

We could confirm the structure dependence of the performance of the silicon strip detector with APV25 readout, and SVD upgrade will be developed based on this result.

Contents

List of Figures

Chapter 1

Introduction

Many precise experiments have confirmed the Standard Model (SM) for the past 30 years. However, the SM is not the complete theory which includes too many parameters. The hierarchy of quark and lepton masses and the flavor mixing matrices also suggest hidden mechanism at higher energy scale.

There are many theories beyond the SM. One way to discover a new physics beyond SM is the energy-frontier collider experiment at TeV energy scale. To achieve that energy scale, Large Hadron Collider (LHC) and International Linear Collider (ILC) are planned. Another way is the high-luminosity collider experiment to measure the phenomena with small amplitude. The Belle experiment are conducted for this purpose.

In the Belle experiment, CP violation is studied through B mesons decays. The KEKB for the Belle experiment is e^+e^- asymmetric-energy collider. It has the highest collision rate of the beam (luminosity) in e^+e^- colliders, and achieved the peak luminosity of $1.71 \times 10^{34}\mathrm{cm}^{-2}\mathrm{s}^{-1}$(November-15-2006). Since the branching fractions of the rare B meson decays for the CP violation study is quite small, large integrated luminosity, corresponding to a large data set, is required. The KEKB will increase the luminosity more and more, and more

beam-induced background is brought to the Belle detector, especially to the innermost detector SVD.

The Silicon Vertex Detector (SVD) precisely detects the decay vertex of B mesons for the measurements of the time-dependent CP asymmetries. The resolution of the measured vertices is required good enough to measure the $B^0\bar{B}^0$ mixing oscillation. Because SVD is placed at the innermost of the Belle detector, it is exposed by much beam background.

According to the plan of the luminosity increase at the KEKB, the ratio of hit channel to all channel (occupancy) of the SVD at innermost layers will be up to 30% in 2008 due to the increased beam background. To cope with this problem, we like to introduce a readout chip such as APV25 whose peaking time ($\sim$50ns) is 16 times as fast as current readout chip VA1TA.

However, it is suggested that the readout with faster peaking time causes much larger noise from detector capacitance. Then a prototype sensor with 5 different strip-configurations are prepared for the design of new DSSD, which is expected to have enough performance with APV25 readout.

We did a beam test (4GeV π^- beam) to evaluate the performance of the prototype sensor with APV25 readout. As the results of beam test, I will show the hit-finding efficiency, signal to noise ratio, and spatial resolution.

The purpose of this thesis is to evaluate and study the performance of the new-designed sensor with APV25 readout for the SVD upgrade. I will describe the outline of the Belle experiment in Chapter 2, the detail of the SVD and its upgrade in Chapter 3, the configuration of the sensor used by research in Chapter 4, results of beam test in Chapter5, and the conclusion of this research in Chapter 6.

Chapter 2

Belle experiment

In this chapter, I describe the physics motivation and detail of Belle experiment.

2.1 Physics motivation

The main purpose of the Belle experiment is to determine the parameters of the quark mixing matrix, so-called *Cabibbo-Kobayashi-Masukawa* (CKM) matrix, which projects one set of states onto the other.

According to the present astrophysics, it is supposed that this universe was started with the Big-bang and the same number of particles and anti-particles are generated. However, the universe of anti-particles can not be found. We can expect that the behavior of particles and anti-particles are different and only particles have survived. What is the difference? The hint to solve this is CP violation, and the CP violation can be explained by CKM matrix and *Kobayashi-Masukawa* theory.

2.1.1 CP violation

There are three discrete transformation:
C(Charge-conjugation), P(Parity-inversion), and T(Time-reversal) transformation. C transformation reverses the sign of charge and the direction of the

electric-magnetic field. P transformation is the simultaneous flip in the sign of all spatial coordinates. T transformation reverse the time propagating direction.

C and P symmetry was known to be violated in the weak interaction, but it was believed that C symmetry could be combined with P transformation to preserve a combined CP symmetry.

However in 1964, the group of Christenson,, Cronin, Fitch and Turlay discovered the violation of even this symmetry in the K^0-$\bar{K^0}$ decay experiment. K^0 and $\bar{K^0}$ are different in strangeness, which is not preserved in the weak interaction. In the K^0 and $\bar{K^0}$ decay mode, there are two final states, two π and three π, whose CP eigenvalue are +1 and -1 respectively. Then define the initial state as below,

$$|K_1>\equiv \frac{1}{\sqrt{2}}(|K^0>+|\bar{K^0}>) : CP|K_1>=|\bar{K_1}> \tag{2.1}$$

$$|K_2>\equiv \frac{1}{\sqrt{2}}(|K^0>-|\bar{K^0}>) : CP|K_2>=-|\bar{K_2}> \tag{2.2}$$

where the phase is defined as below.

$$CP|K^0>\equiv|\bar{K^0}>, CP|\bar{K^0}>\equiv|K^0> \tag{2.3}$$

If CP symmetry is preserved, K_1 decays to two π and K_2 to three π. They discovered that after K_1 finished its decay, about 0.2% of K_2 decays to two π. This means that there is $|K_1>, |K_2>$ mixing, that is to say, there is the interaction which violates the CP symmetry.

2.1.2 CKM matrix

The most promising model to explain CP violation is Kobayashi-Masukawa theory. According to this theory, if six kinds of quarks exist, CP violation can be derived through the mixture between quarks within the Standard-model framework of modern particle physics.

The interaction Lagrangian of 6 quarks and $W^{\pm}$ is described as below,

$$L_{int} = \frac{g}{\sqrt{2}} \left((\bar{u}, \bar{c}, \bar{t})_L \gamma^\mu W^- V_{KM} \begin{pmatrix} d \\ s \\ b \end{pmatrix}_L + (\bar{d}, \bar{s}, \bar{b})_L \gamma^\mu W^- V_{KM} \begin{pmatrix} u \\ c \\ t \end{pmatrix}_L \right) \tag{2.4}$$

where V is the 3×3 unitary matrix called *Cabibbo-Kobayashi-Masukawa* (CKM) matrix. V_{KM} is shown below,

$$V_{KM} \equiv \begin{pmatrix} V_{ud} & V_{us} & V_{ub} \\ V_{cd} & V_{cs} & V_{cb} \\ V_{td} & V_{ts} & V_{tb} \end{pmatrix}_L = \begin{pmatrix} 1 - \frac{\lambda^2}{2} & \lambda & A\lambda^3(\rho - i\eta) \\ -\lambda & 1 - \frac{\lambda^2}{2} & A\lambda^2 \\ A\lambda^3(1 - \rho - i\eta) & -A\lambda^2 & 1 \end{pmatrix}_L \tag{2.5}$$

where A, ρ, and η are real numbers. λ and A are known experimentally.

The constraints of unitarity ($V_{KM}^\dagger V_{KM} = 1$) of the CKM-matrix on the diagonal terms can be written as for all generations i.

$$\sum_j |V_{ii}|^2 = 1 \tag{2.6}$$

This implies that the sum of all couplings of any of the up-type quarks to all the down-type quarks is the same for all generations. The remaining constraints of unitarity of the CKM matrix can be written in the form

$$\sum_k V_{ik} V_{jk}^* = 0 \tag{2.7}$$

For any fixed i and j, this is a constraint on three complex numbers, one for each k, which says that these numbers form the vertices of a triangle in the complex plane. There are six choices of i and j, and hence six such triangles, each of which is called an unitary triangle. Their shapes can be very different, but they all have the same area, which can be related to the CP violating phase. The area vanishes for the specific parameters in the standard model for which there would be no CP violation. The orientation of the triangles depend on the phases of the quark fields.

The Goals of the Belle experiment is to observe and understand the CP violation in B meson decays. Then, unitality applied to first and third columns yields of CKM matrix is,

$$V_{ud}V_{ub}^{*} + V_{cd}V_{cb}^{*} + V_{td}V_{tb}^{*} = 1 \tag{2.8}$$

and the unitarity triangle is shown in Figure2.1

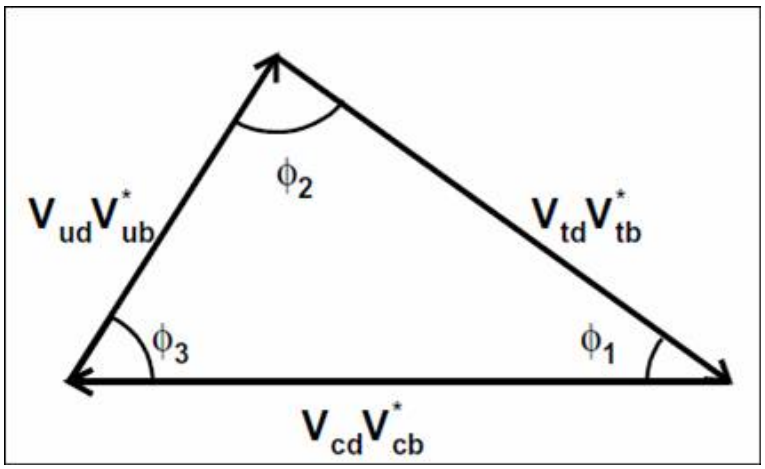

Figure 2.1: The unitarity triangle

Since the three sides of the triangles are open to direct experiment, as are the three angles, a class of tests of the standard model is to check that the triangle closes. This is one of the most important purpose of Belle experiments.

2.2 KEKB accelerator

KEKB (Figure2.2), located in Tsukuba Japan, is the e^+e^- asymmetric-energy collider with a circumference of about 3km. Since it is used for production of a large number of B mesons, it is called *B-Factry*.

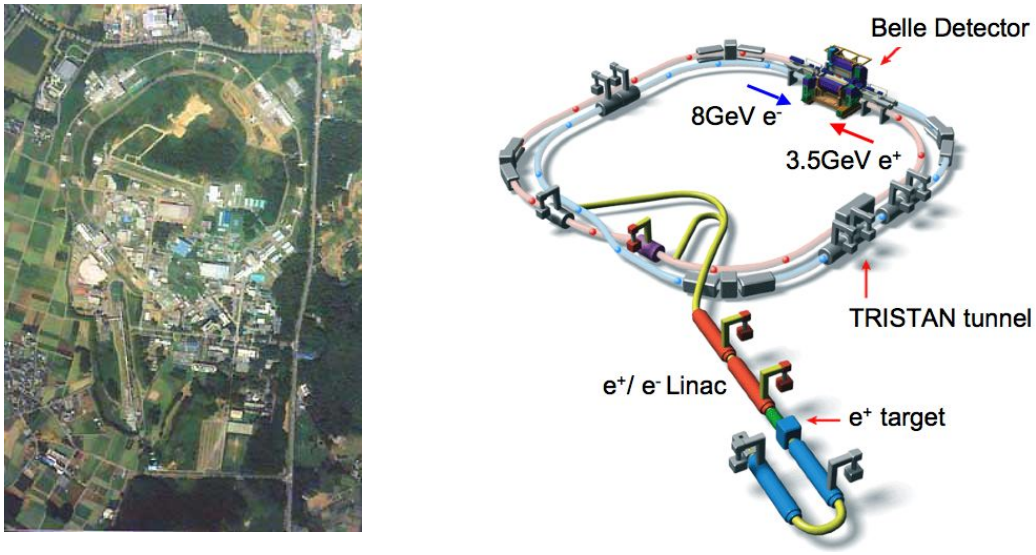

Figure 2.2: KEKB accelerator

The KEKB accelerator has two rings in a tunnel which is used for TRISTAN. The energy of electron and positron beams are 8GeV and 3.5GeV respectively, so that the center of mass energy becomes equal to the (4S) resonance energy. In the Belle experiment, CP violation is measured as the asymmetry of the distribution of the proper time difference between B^0 and $\bar{B}^0$ decays. This time difference is too short (∼1ps), and it is quite difficult to measure the difference directly. In the Belle experiment, because of the energy asymmetry, the center of mass system are boosted by a Lorentz factor of $\beta\gamma = 0.425$. Therefore we can measure the time differences (∼1.5ps) by determining the decay position difference of $\sim 200\mu$m (Figure2.3).

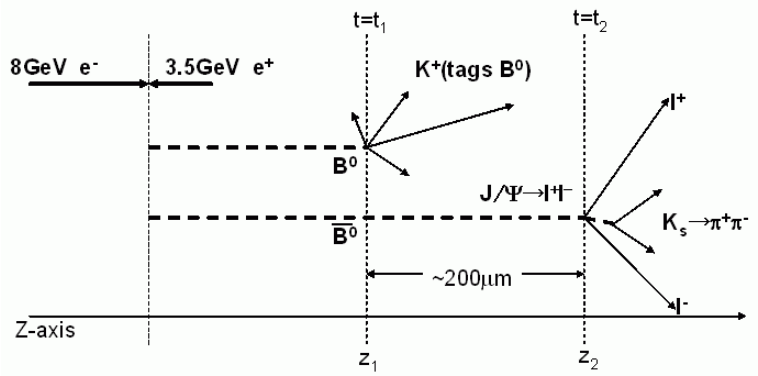

Figure 2.3: Decay diagram of B mesons

On the other hand, a large number of B mesons are required for this study since the probability of a B meson decay to a CP eigenstate is extremely low with $10^{-4} \sim 10^{-5}$. Then for the KEKB accelerator, the high luminosity beam is required. The peak luminosity is $1.71 \times 10^{34}\mathrm{cm}^{-2}\mathrm{s}^{-1}$(November-15-2006), which is the world record. Figure2.4 shows the luminosity history of the KEKB compared with the PEP-II at the BaBar experiment, which is our rival experiment at SLAC, USA .

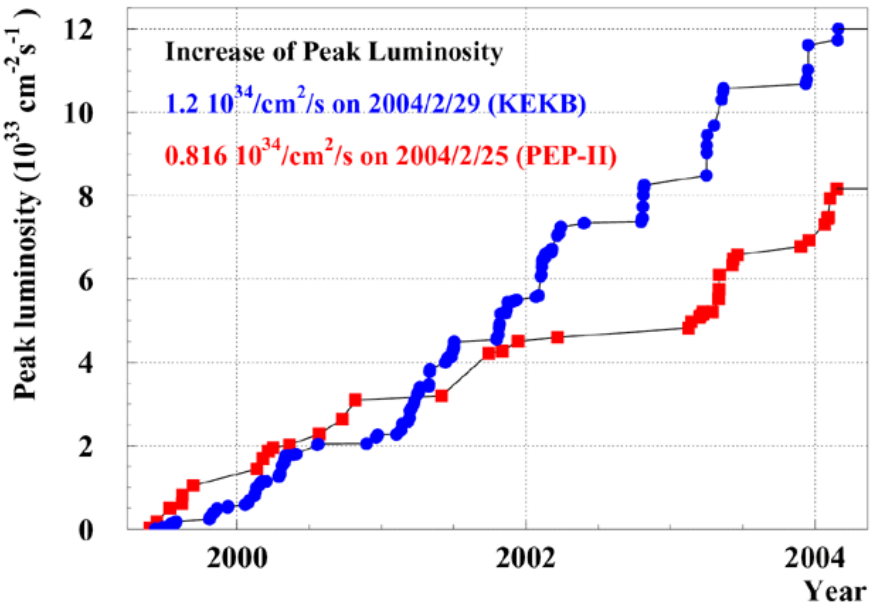

Figure 2.4: Luminosity comparison between KEKB and PEP-II

KEKB people will plan to install crab cavities, which effectively creates a head-on collision, for both rings in the early 2006. Peak luminosity will be more than doubled. To further extend reach for the new physics search, SuperKEKB is planned. Figure2.5 shows the plan of the KEKB accelerator upgrade.

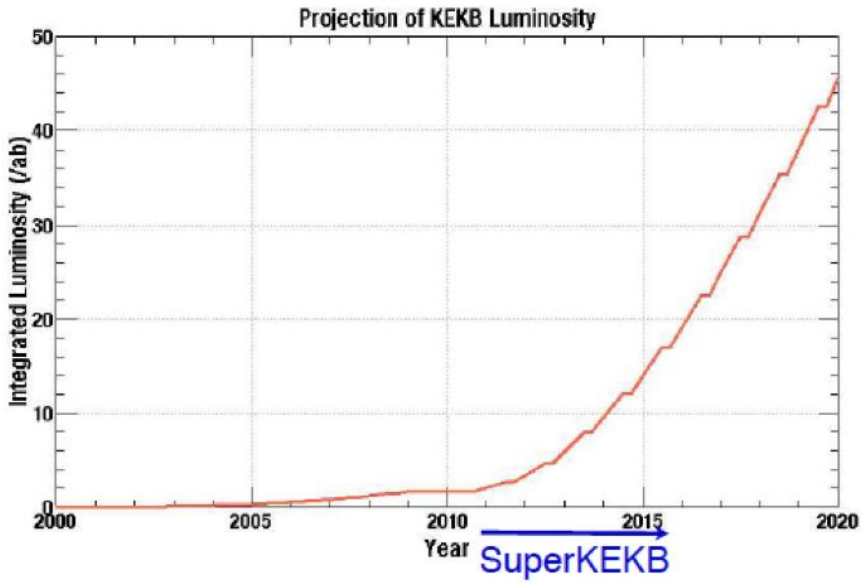

Figure 2.5: The KEKB upgrade (integrated luminosity)

2.3 Belle detector

The Belle detector consists of several sub-detectors as show in Figure2.6. It has a cylindrical shape surrounding the beam pipe: from an inner part, Silicon Vertex Detector (SVD), 50-layer Central Drift Chamber (CDC), Aerogel Cerenkov Counter (ACC), Time-Of-Flight counters (TOF), Electromagnetic Calorimeter (ECL), K_L/μ detection system (KLM). In the Belle experiment, the coordinates in the vicinity of the collision point are defined in cylindrical coordinates: z-axis is defined as a direction anti-parallel to the positron beam and r-ϕ plain is vertical to the z-axis.

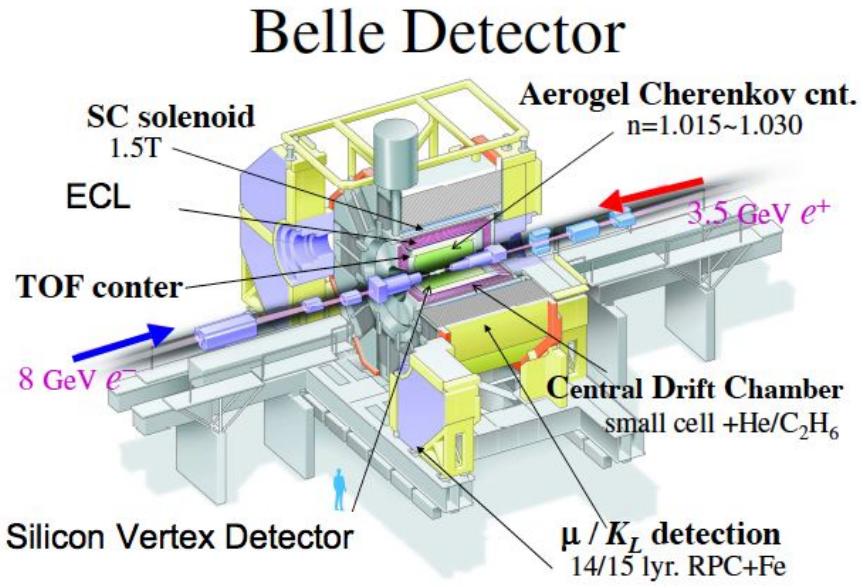

Figure 2.6: Belle detector

Silicon Vertex Detector (SVD)

A detail of the SVD will be described in Chapter3. The SVD is a sensitive semiconductor detector for the vertex position, which is located at the most inner position in the Belle detector. We need to measure the decay position differences between two B mesons to detect CP violation of B mesons. Since an average decay length of a B meson is about 200μm, position resolution less than 100μm is required for the SVD.

Central Drift Chamber (CDC)

The primary purpose of the CDC is to detect charged particle tracks and to reconstruct their momenta. The position resolution of the tracks is a few millimeters for the z direction and about 130μm for the r-ϕ direction, and P_t resolution is $\sim 0.19 P_t \oplus 0.30/\beta$ %. The trajectories of charged particles detected in the CDC are extrapolated to the SVD, and initiating the SVD tracking. CDC also gives particle identification by measuring the energy loss in it. The position information is used for a trigger signal.

Aerogel Cherenkov Counter (ACC)

The role of ACC is particle identification, specifically the ability to distinguish π and K mesons. A particle can be identified by the information whether it emits Cherenkov radiation or not. While relativity holds that the speed of light in a vacuum is a universal constant (c), the speed of light in a material may be significantly less than c. Cherenkov radiation is emitted when a charged particle exceeds the speed of light in a material. The Silica-aerogel has a reflactive index between 1.01 and 1.03, and the momentum range of the particle identified is between 1.2GeV/c and 3.5GeV/c.

Time Of Flight counters (TOF)

The TOF, which is composed of 128 plastic scintillators and 256 photo-multipliers, is used for the particle identification. For a 1.2 m flight path, the TOF system with 100 ps time resolution is effective for particle momenta below about 1.2 GeV/c, which encompasses 90% of the particles produced in Upsilon(4S) decays. TOF also has other sets of scintillation counters, and they are used to generate the trigger signal. A pre-trigger to hold SVD signal is generated by TOF trigger.

Electromagnetic Calorimeter (ECL)

The main purpose of ECL, which is composed by a highly segmented array of CsI(TI) crystals, is to detect photons from B meson decays with high efficiency and good energy resolution. ECL is also used for the measurement of the luminosity using Bhabha scattering. ECL covers a wide energy range from 20 MeV to 8 GeV.

K_L/μ detection system (KLM)

The KLM is able to detect K_L's and muons with high efficiency over abroad momentum range greater than 600 MeV/c. The KLM is placed at the most outside of the Belle detector and consists of high resistance plate chambers and iron plates. Hadron shower occures if K_L mesons interacts with the KLM, so the muons can be identified as a particle which goes through all the iron layers. The signal from KLM is also used for the trigger generation.

Chapter 3

The Silicon Vertex Detector (SVD)

To observe time-dependent CP asymmetries in the decays of B mesons, SVD is required the measurement of the difference in z-vertex positions for B meson pairs with a precision of $\sim$100 μm.

3.1 The current SVD

Since the SVD is located at about 3cm from the beam line, the radiation level of the SVD is quite high. To cope with this difficulty, the SVD upgrade have been performed three times. The SVD operating at present is called the SVD2 and it was installed in the summer of 2003 (Figure3.1).

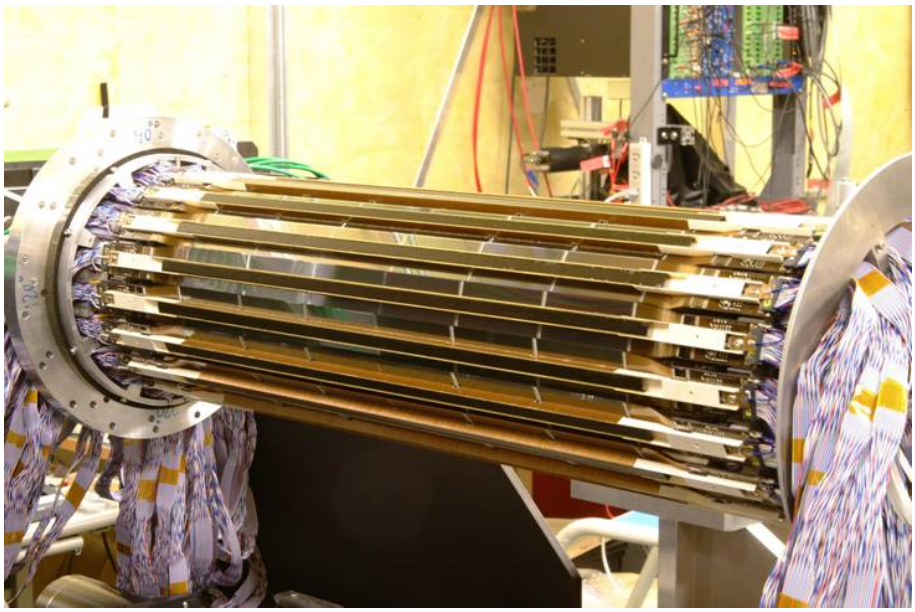

Figure 3.1: SVD2

3.1.1 Structure

Figure3.2 and Figure3.3 shows $r-\phi$ and z views of the SVD2. SVD consists of 4 layers of the detector ladders (Figure3.4) around the beam pipe. In a ladder, there are two or more DSSDs (described in next subsection). Parameters of SVD2 is shown in Table3.1

When charged particles go through SVD, we find the hit position at each layer. Then we can reconstruct charged tracks and measure the decay vertex of B mesons.

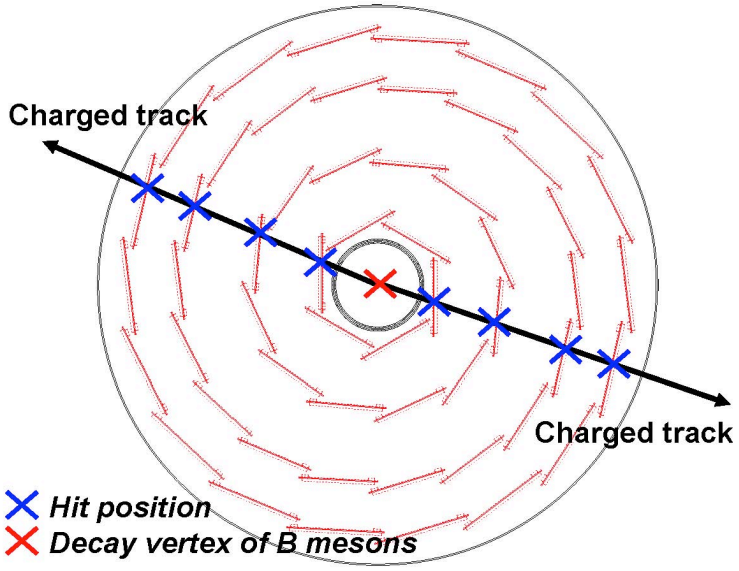

Figure 3.2: SVD2,$r-\phi$ direction diagram

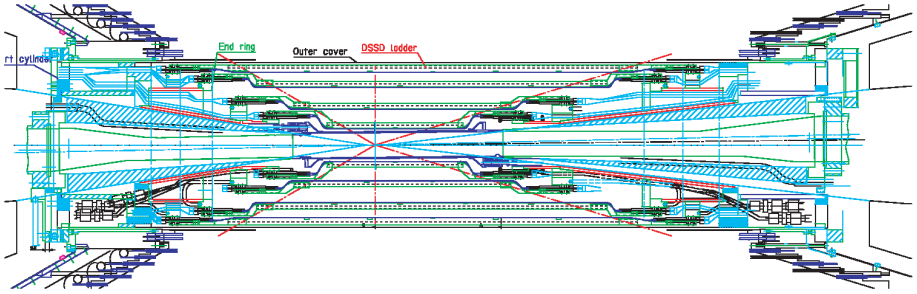

Figure 3.3: SVD2,z direction diagram

Figure 3.4: Ladder structure

Beampiperadius[mm]	15
Numberof layers	4
Numberof DSSD ladders in layers 1/2/3/4	6/12/18/18
Numberof DSSDs in a ladder in layers 1/2/3/4	2/3/5/6
Radii of layers [mm] inlayers 1/2/3/4	20.0/43.3/70.0/88.0
Angular coverage (acceptance)	$17^\circ < \theta < 150^\circ$ (0.92)
Active area $[mm^2]$ per sensor	76.8×25.6 (73.8×33.3 for Layer-4)
Total number of channels	110592
Strip pitch [μm] for P-side(z)	75(73 for Layer-4)
Readout pitch [μm]	150(146 for Layer-4)
Strip pitch [μm] for N-side(r-ϕ)	50(65 for Layer-4)
Readout pitch [μm]	50(65 for Layer-4)
DSSD thickness [μm]	300
Total material at $\theta = 90^\circ$ [X_0]	2.6
Readout chip	VA1TA
Readaout scheme	Track and Hold
Intrinsic DAQ deadtime/event [μs]	25.6

Table 3.1: Parameters of SVD2

3.1.2 Double-sided Silicon Strip Detector (DSSD)

In each layer, we are using Double-sied Silicon Vertex Detector (DSSD), which is a semiconductor detector fabricated by Hamamatsu Photonics with 300μm thickness.

Figure3.5 shows DSSD structure. It consists of 512 N^+ strips in one side (N-side) and 1024 P^+ strips in the other side (P-side), which are mutually perpendicular. Since the silicon bulk is made from N type semiconductor, the P-stops is implanted around the N^+ strips to insulate neighboring strips electrically. At the operation, the bias voltage (N-side +40V: P-side -40V) is applied to the DSSD for the complete depletion.

When a charged particle passes through the DSSD, the particle deposits its energy in the sensor, and electron-hole pairs are generated along the path. Since the electrons have negative charge, it will be collected by N^+ strips, and

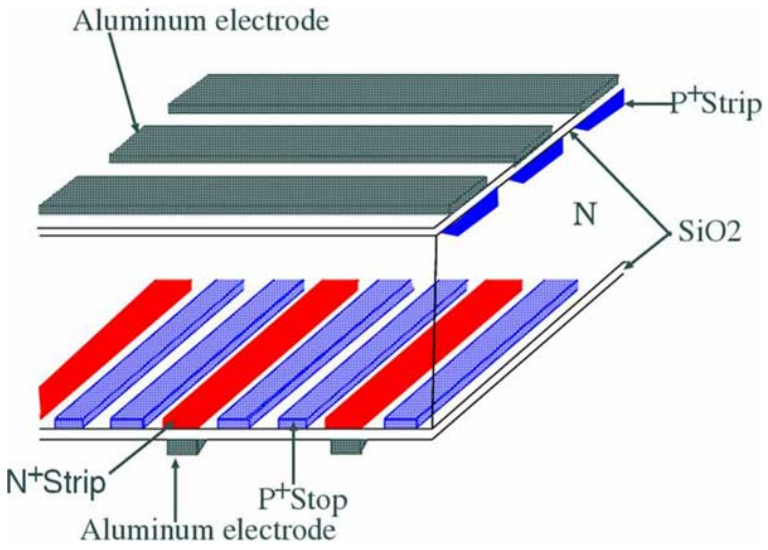

Figure 3.5: DSSD structure

holes will be collected by the P^+ strips. They are observed as electric signals, and we can obtain two dimensional position of the particle with the mutually-perpendicular strips: z direction is read by P-side and r-ϕ direction is read by N-side. When a charged particle penetrates with a large incident angle, the signal are distributed with the sequential strips. In this case, the position is calculated by a center of gravity method.

Table3.2 shows characteristics of the DSSD used by the SVD2. Because of the sensor size, the number of strips in the P-side is twice that in N-side.

	Layer1-3		Layer4	
	P-side	N-side	P-side	N-side
Chip size [mm]	$79.6 \times 28.4 \times 0.3$		$76.4 \times 34.9 \times 0.3$	
Active area [mm]	76.8×25.6		73.8×33.3	
Strip pitch [μm]	75	50	73	65
Number of strips	1024	512	1024	512
Readout pitch [μm]	150	50	146	65
Strip width [μm]	50	10	55	12
Readout electrode width [μm]	56	10	61	10

Table 3.2: Characteristics of DSSD

3.1.3 VA1TA

In the SVD2, signals from DSSD is read by a LSI chip called VA1TA which has 128 input channels with a peaking time of 800ns. Since there are 512 readout strips at one side in a DSSD, they are read by four VA1TA chips. These four chips are integrated on a hybrid circuit. Figure3.6 shows a picture of the VA1TA and the hybrid.

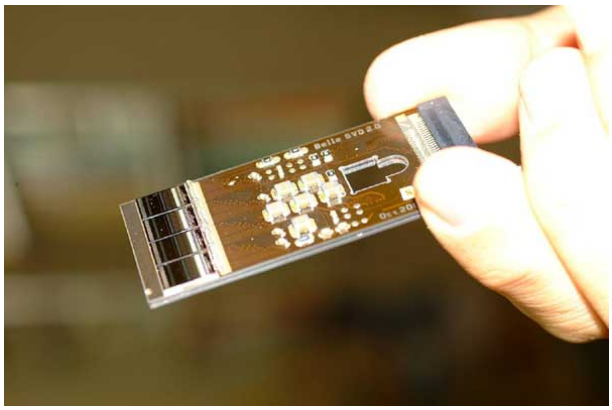

Figure 3.6: hybrid picture

Figure3.7 shows the VA1TA diagram. The VA1TA consists of VA in the analog amplifier part and TA in the trigger part. When a charged particle penetrates the DSSD and the electric charge is generated on the strips, the charge is converted into the voltage with a preamplifier and then integrated by a shaper. Then, the signals of 128 channels are read by a single line through a multiplexer.

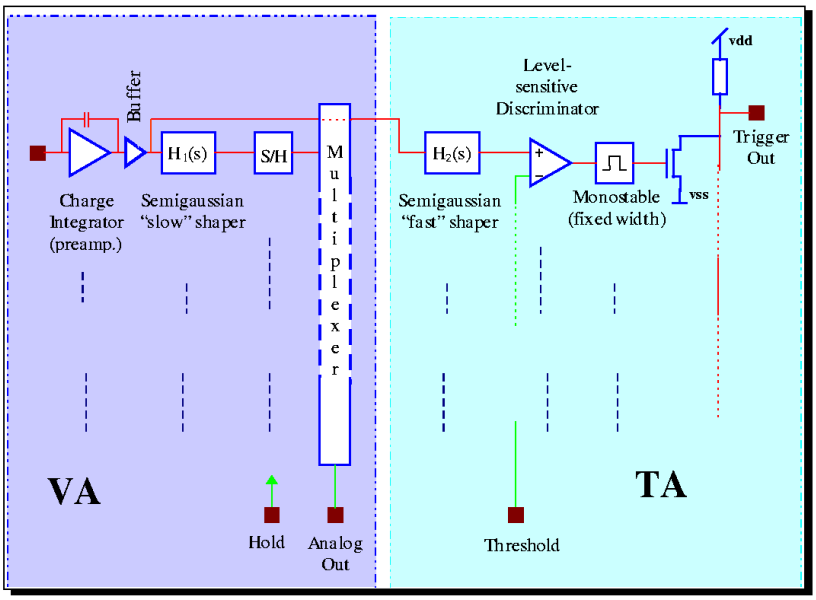

Figure 3.7: VA1TA diagram

3.1.4 Readout system

Figure3.8 shows the readout system used in the SVD2. The function of each module is explained as follows.

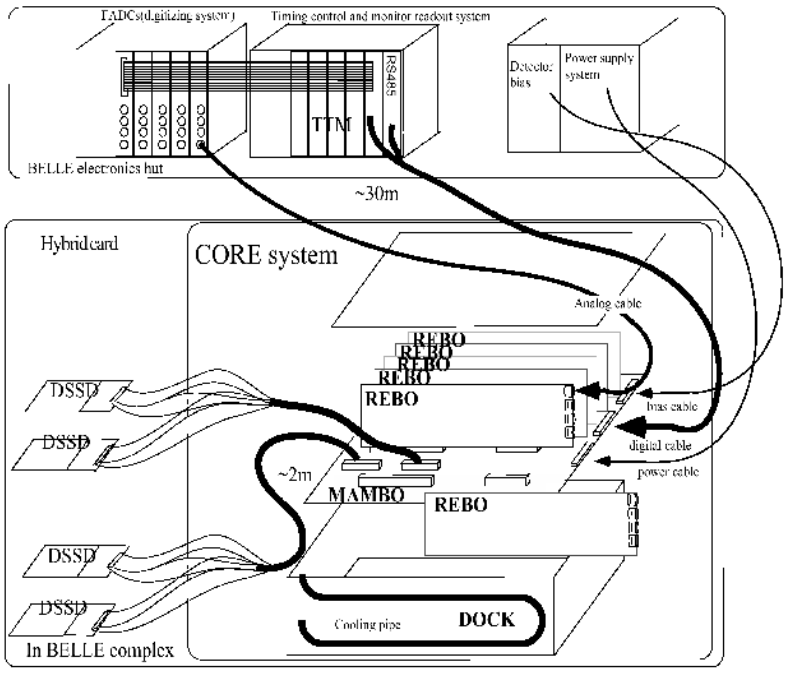

Figure 3.8: SVD readout system

CORE (COntrol and REpeater) system It consists of six repeater boards called REBO. The REBO sends the control signal or receives the analog signals from the VA1TA. MAMBO is the mother board which controls the REBO. The MAMBO also controls the power supply. The CORE system is encapsulated in a copper cooling box and it is called DOCK. The REBO is able to read 4 hybrid data, and six REBOs and one MAMBO is placed in the DOCK. Total ten DOCKs are used for the readout of the SVD.

FADC (Flash ADC) A flash ADC (FADC) is a 9U VME module that converts the analog signal from REBO into the digital signal at 5MHz and send it to PC via a PCI control. One FADC can read six hybrid data. In the SVD2, there are thirty-six FADC modules in total, and eighteen module out of them are used for the N-side readout and the other eighteen

are used for the P-side readout.

TTM (Trigger Timing Module) TTM is a 6U VME module that controls the trigger signal and the DAQ system. TTM can send the signal such as ADC start, ADC stop, busy, and 4 bit event tag to the REBO and FADC, and it monitors and controls the readout cycle of the data. There are eleven TTM modules in total.

Power supply Power supply provides both High Voltage (H.V) and Low Voltage (L.V). The H.V is the bias voltage applied to the DSSDs for the depletion. The L.V is used for the front-end electronics. Each one of H.V and L.V supply is utilized for the one DOCK, and there are ten modules in total.

DAQ system Twelve PCs in total are used in the DAQ system of the SVD. It reads the data sent from FADC via the PCI bus. And then, the sparsified data are sent to the Belle event builder. One PC has three PCI boards and can read the data for three FADC modules.

3.1.5 Performance

The typical trigger rate is ∼400Hz and the average occupancy of the SVD is around 3 %. Under these conditions, the performance of SVD2 is good enough as summarized in Table3.3.

S/N	>16
Occupancy [%] in layers 1/2/3/4	10/3.5/2.0/1.5
Hit-finding efficiency [%]	90
Impact parameter resolution [μm] for dz	$26.3 \bigoplus 32.9/(p\beta(\sin\theta^{5/2})$
Impact parameter resolution [μm] for dz	$17.4 \bigoplus 34.3/(p\beta(\sin\theta^{3/2})$

Table 3.3: Parameters of SVD2

Because the technology of KEKB accelerator is developing, SVD2 will not be able to retain its performance. Then we need to upgrade the SVD. I will describe the upgrade in next section.

3.2 Upgrade of the SVD

As described in section2.2 (Figure2.5), the luminosity of the KEKB will increase. In the present schedule, it will increase by three times in 2007. The SVD will be exposed by more radiations, thus beam background level will increases as shown in Figure3.9.

The *occupancy*, which is defined as the ratio of hit strips to all strips, increases proportional to the background level. Figure3.10 shows the hit-finding efficiency as a function of *occupancy* in the first layer. When occupancy increases, it will be difficult to find collect hits.

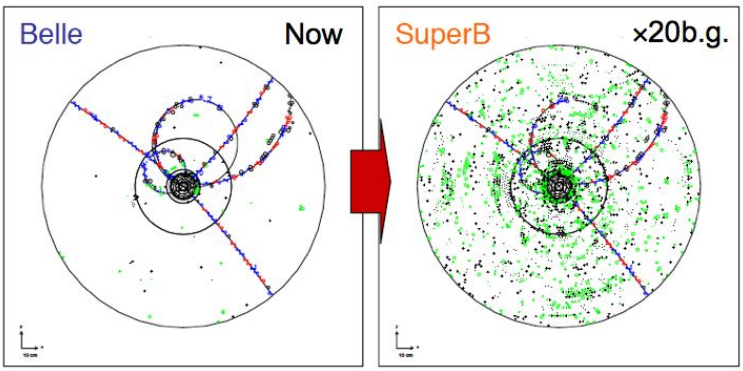

Figure 3.9: Belle event-displays comparing current and 20 times higher one

To cope with this problem, we like to introduce a readout chip such as APV25, which has a faster peaking time (∼50ns). We replaced the readout in the first and second layer ladders, and the new SVD after this upgrade is called SVD3. Since the peaking time of APV25 is 1/16 as fast as that of the present readout chip VA1TA (∼800ns), the occupancy of the SVD is expected to be

reduced by 1/16. Details of the APV25 will be described in next section.

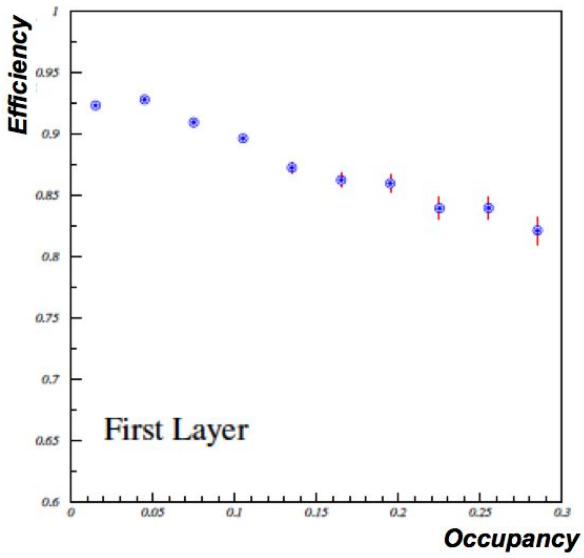

Figure 3.10: Hit-finding efficiency as a function of *occupancy* in the first layer

3.2.1 APV25

The APV25, with128 input channels, has been developed for a silicon detector used at CMS. The feature of APV25 different from current readout VA1TA is as below:

- Faster peaking time (∼50ns)
- Pipeline memory and sequencer

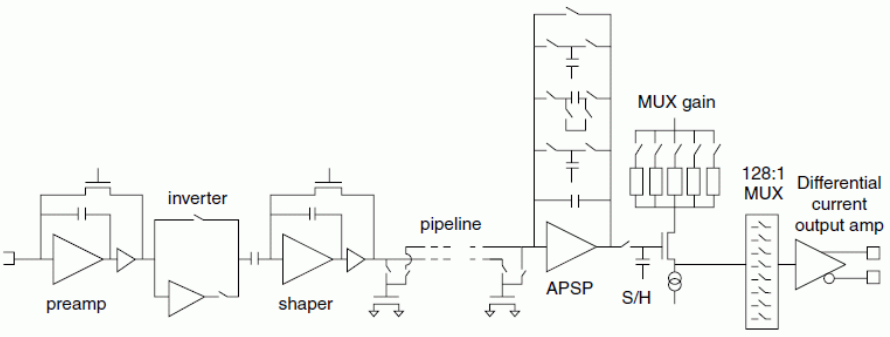

Figure 3.11: APV25 block diagram

As shown in Figure3.11, APV25 consists of a preamplifier, shaper, pipeline and multiplexer. When the signal fed to the APV25 goes through a preamplifier to a shaper, the signal is amplified and shaped with peaking time T_p=50ns.

The shaper output is sampled at clock intervals and stored in the pipeline. The pipeline of the APV25 is a ring buffer which has 192 cells with cycling write and read pointers. The signal stored at the pipeline is read after a certain constant latency time. The latency time between the signal input and the trigger is more than 4μs with 40MHz clock frequency. APV25 has the sequencer that can generate a series of subsequent APV triggers initiated by a single hardware trigger. By using this feature, a sequence of samples separated by a single clock cycle can be obtained (multi-peak mode). This can be used to effectively get subsequent samples of the shaping curve from particle signal. The output signal from one APV chip in multi-peak mode is shown in Figure3.12.

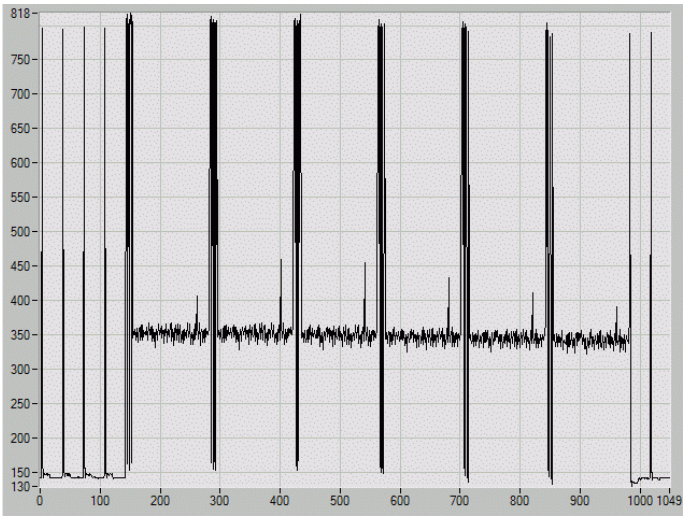

Figure 3.12: Output signal from APV25 in a 6 sample multi-peak mode

3.3 Necessity of new DSSD

Because the noise from a semiconductor detector greatly depends on the detector capacitance in the case of short peaking time, it is expected that the introduction of APV25 causes large noise to the current DSSD.

The intrinsic noise of a semiconductor detector is mainly caused by the detector leakage current and electric capacitance. The formula of noise from the readout chip is,

$$[Intrinsic\ noise] = N_{Capa} \oplus N_{Leak}$$

where N_{Capa} and N_{Leak} are the noises caused by the detector-capacitance and leakage-current respectively, which are represented as follow,

$$C_{Leak} \propto \sqrt{I_{Leak} T_{Peak}}, \tag{3.1}$$

$$C_{Capa} \propto \frac{C_{Load}}{\sqrt{T_{Peak}}}, \tag{3.2}$$

where I_{Leak}, C_{Load}, T_{Peak} is the leakage-current, the load capacitance of one strip, and the peaking time of shaping curve.

Since the current DSSD is designed to be minimized the radiation damage, the strip width is maximized, therefore the detector-capacitance is large. When we introduce APV25 that has a faster peaking time, the N_{Capa} term will become dominant (Formula(3.1), (3.2)). Then, if we use the current DSSD with APV25, the intrinsic noise will become very large, and this degrade the sensor performance.

To solve this difficulty, we need new DSSD for capacitance reduction. Since the capacitance of the N-side is especially larger than P-side because of the P-stop, we prepared a prototype of N-side Single-sided Silicon-strip Detector (SSD)

with 5 different strip-configuration. I will show the detail of the prototype in next chapter.

Chapter 4

Test sensor

The test sensor is fabricated by HPK. It is a N-side single-sided strip detector (SSD), since the capacitance of the N-side is especially larger than P-side because of the P-stop.

4.1 Structure of the test sensor

The blue print of this sensor is shown in the Figure4.1. The test sensor has 5 regions of different structure.

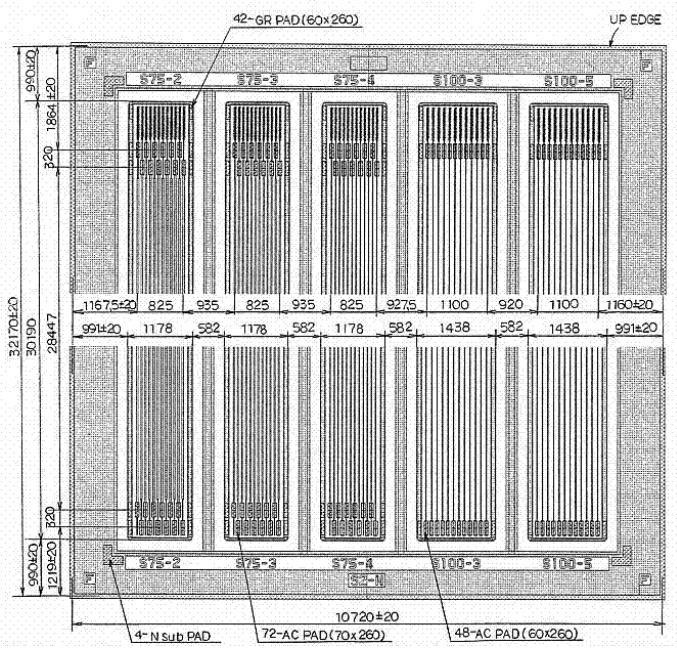

Figure 4.1: N-side SSD blue print

The parameters of each region are shown in Table4.1. 5 regions are different in strip pitch, strip width, and P-stop gap. Note that readout pitch in 75μm-pitch regions is twice as wide as strip pitch, that is to say, strips in the regions are read alternately.

	S75-2	S75-3	S75-4	S100-3	S100-5
Sensor size [mm]	10.7×32.2				
Active area [mm]	8.3×28.4			11.0×28.4	
Strip pitch [μm] (A)	75			100	
Readout pitch [μm]	150			100	
Number of strips	12				
N-strip width [μm] (B)	32	24	12	12	12
P-stop width [μm] (C)	12	12	7	35	10
N-strip-P-stop gap [μm] (D)	6				
P-stop gap [μm] (E)	7	15	37	6	56

Table 4.1: SSD parameters

The cross section view of the SSD is shown in Figure4.2. In N-side, there are N-strips, and P-stops to insulate neighbor strips each other in N-strip. In P-side, the whole region is implanted by P^+.

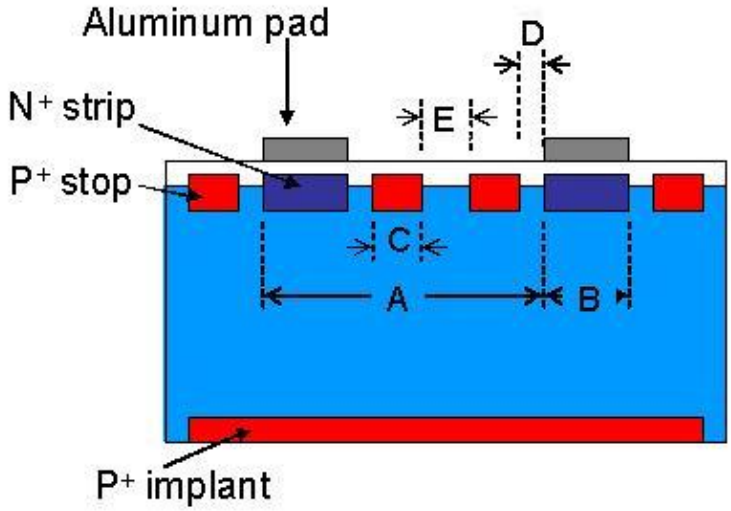

Figure 4.2: The cross section view of the test sensor

The detail of one region in the sensor is shown in Figure4.3. In P-side, there are two slits perpendicular to strip direction. These slits are used for laser scan of the sensor. And there are individual bias pads through which we are able to apply bias voltage to individual regions.

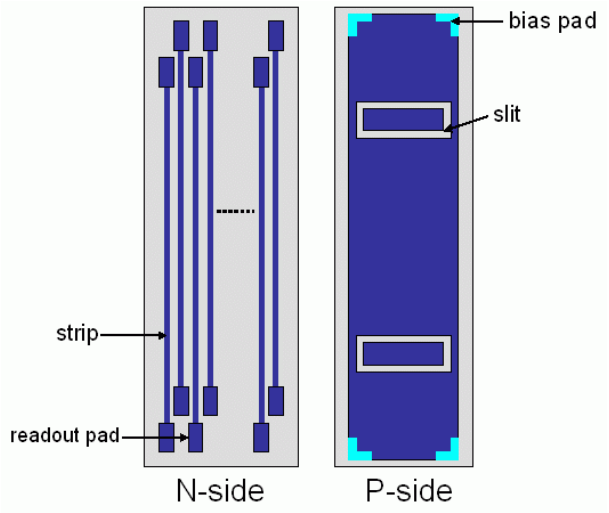

Figure 4.3: The detail of one area in the test sensor

4.2 Test sample

Figure4.4 shows a picture of a test sample. The test sample consists of same 2 test sensors, a bias line for the bias voltage, and a hybrid with 4 APV chips.

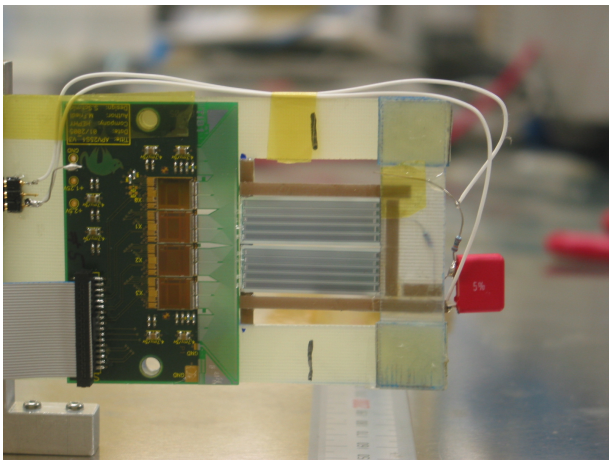

Figure 4.4: Picture of a test sample

The negative bias voltage(0 to -100V) is applied from the P-side of the test sensor. Sensor strips are connected to the APV25 chip. This test sample was used for the beam test described in Chapter5.

4.3 DAQ system of APV25 readout

Figure4.5 shows a DAQ system of APV25 readout. The output from the APV25 chips are fed to APVDAQ through the AC Repeater.

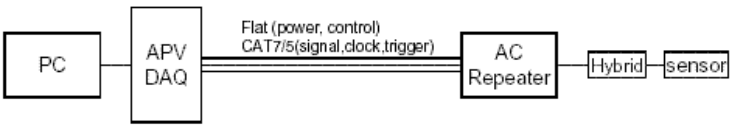

Figure 4.5: APV DAQ system

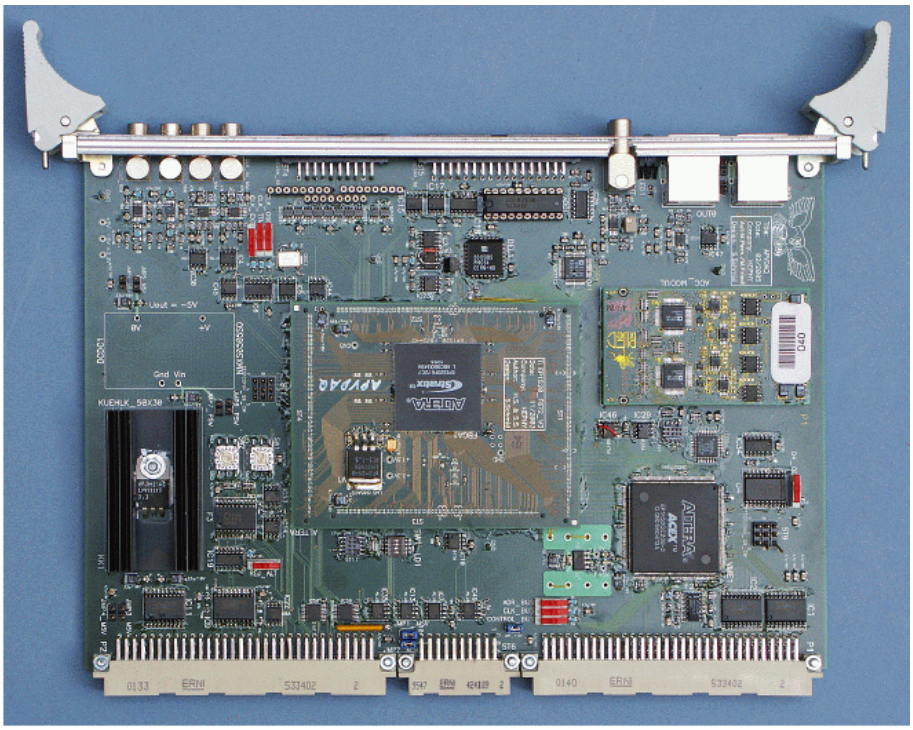

Figure 4.6: APVDAQ

The APVDAQ (Figure4.6) is a 6U VME module used for the control and readout from the APV25 chip. It consists of a Stratix Altera, a VME protocol Altera, an ADC daughter board and supplemental electronics. On the front panel of APVDAQ, there are an analog signal input and an output for the controls (clock, trigger etc.), and these are connected to the Repeater with flat cable and CAT7 cables respectively. Furthermore, there are an external clock input and a trigger input on the front panel.

The AC reapeater is an interface between the hybrid and the APVDAQ. It bridges signals to the floating power scheme of the APV chip for clock, trigger, and analog signals.

The control of the DAQ system and readout of the analog data is carried out by a PC. The data acquisition software operates with the LabWindows/CVI

developed by National Instruments. This software is written in the C programming language.

There are several operation types in the data acquisition system. The measurements are mainly performed with two operation modes: Hardware run and Internal calibration scan run. The Hardware run is a normal operation with an external trigger. The Internal calibration scan is used for the sampling of the APV output waveform. From these waveform data, the peaking time and chip gain can be calculated.

In a data acquisition, the VME board and APV are reset first. Next, APV25 chip parameters such as shaping time and number of samples are fixed. And then 600 events of local run (Appendix A) are taken by the internal triggers. These 600 events are used to calculate pedestal and noise. After that, a data acquisition with Hardware run starts.

4.4 Sensor capacitance

Detector capacitance consists of two kinds of DSSD capacitance. One is the interstrip capacitance C_i and the other is capacitance between strip and back plane C_b.

The back plane capacitance C_b is very small compare to C_i because the distance between P and N side, which is about 300μm, is much larger than the strip pitch. So the interstrip capacitance C_i mainly contribute to the detector capacitance. According to the LEP-SI model (Appendix B), C_i is a function of the ratio of the strip width to the strip pitch.

Figure4.7 shows the bias voltage dependence of the interstrip capacitance of each region. In this measurement, 1MHz AC voltage is applied between two

adjoined strips. The bias voltage is applied from P-side and changed from 0 to -100V. The capacitance is measured one hundred times at each voltage and the average is taken.

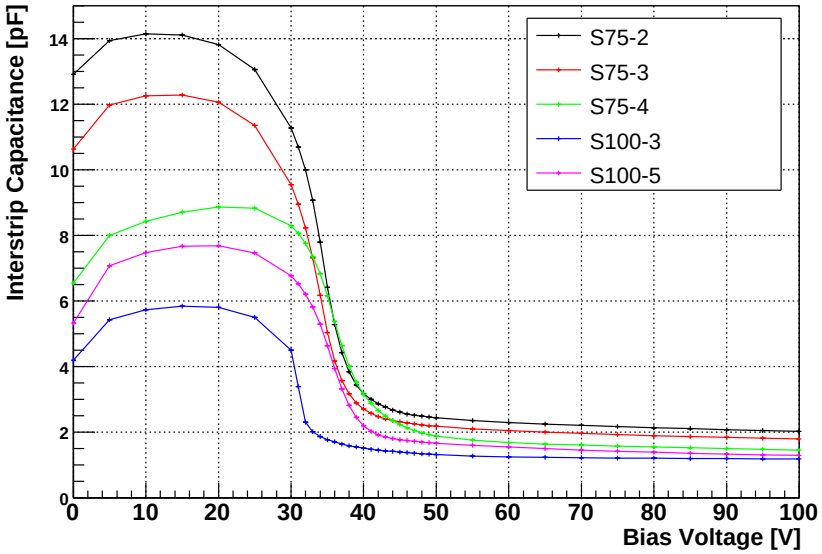

Figure 4.7: The bias voltage dependence of the interstrip capacitance

At the low bias voltage, the interstrip capacitance is large, because a depletion zone is not formed. As the bias voltage increases, the capacitance become small. At 60V or more, a depletion zone is completely formed and the capacitance comes to be minimized.

Table4.2 shows the interstrip capacitance in each region at -60, -80V, -100V bias voltage, and one calculated by LEP-SI model in each region. The region with smaller ratio of the strip width to the strip pitch has smaller capacitance. Therefore the noise cause by load-capacitance is small for the narrow strip width. The measured capacitance is almost same as LEP-SI model.

	S75-2	S75-3	S75-4	S100-3	S100-5
-60V	2.3pF	2.0pF	1.7pF	1.2pF	1.5pF
-80V	2.1pF	1.9pF	1.6pF	1.2pF	1.4pF
-100V	2.0pF	1.8pF	1.6pF	1.2pF	1.3pF
LEP-SI model	2.3pF	2.0pF	1.5pF	1.4pF	1.4pF

Table 4.2: SSD interstrip capacitance

Chapter 5

Beam test analysis

In this chapter, I will describe the detail of the beam test ducted at KEK in December, 2005. The purpose of this test is to measure spatial resolution and hit-finding efficiency of the test sensor with APV25 readout, which is described in chapter4.

5.1 Condition of the beam test

5.1.1 Outline

The beam test was performed at the KEK/PS $\pi 2$ beam line (Figure5.1) in December, 2005. Since the perpendicular 4GeV/c π^- beam are obtained, we can precisely measure the performance of the test sensor as same as that in real operation.

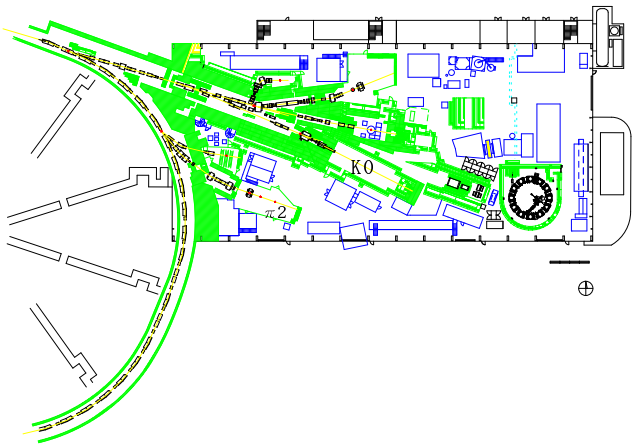

Figure 5.1: The beam line in KEK/PS

5.1.2 Test detector system

A layout and a picture of the test detector are shown in Figure5.2 and Figure5.3.

The test detector of the beam test includes the test sample described in chapter4 and three DSSD ladders. These DSSD ladders are for the telescope, and are the spare of layer-1 ladders of SVD2 but slightly different from the currently operated SVD2 ones: there is no aluminum electnode pad on the floating strip in P-side.

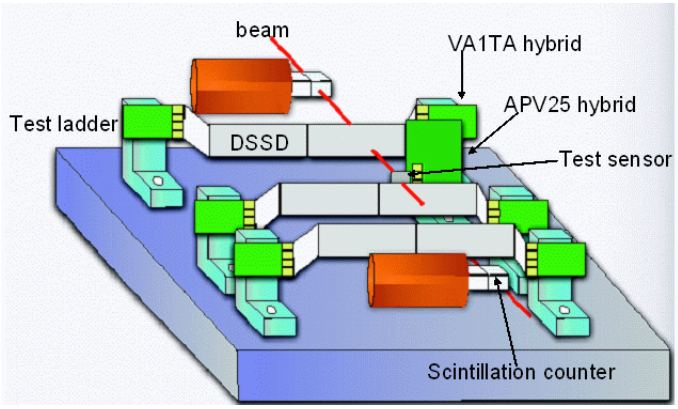

Figure 5.2: Test detector layout

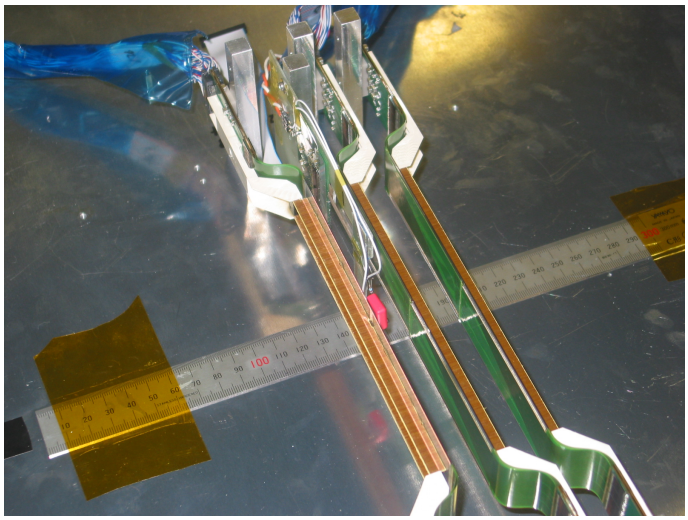

Figure 5.3: Test detector picture

5.1.3 Readout system

Figure5.4 shows a schematic diagram of the readout system at the beam test. We operated the APV25 and VA1TA synchronously as same as we will in SVD3 operation. A test sample is read by the readout of APV25, and three DSSDs are read by the readout of VA1TA. For the readout of the APV25, APVDAQ explained in Section4.3 is used, and for the readout of the VA1TA, the same system as the actual SVD readout described in Section3.1.4 are used.

A trigger signal is generated by taking the coincidence of the signal of two scintillation counters. This signal is fed to the APVDAQ and TTM. After trigger acceptance, a veto signal is issued from both APVDAQ and TTM. By using the veto signal, we can avoid the event slip between APV25 and VA1TA. The VA1TA data has a 4bit event tag. It is also sent to the APVDAQ , and we can match the event between APV25 and VA1TA data acquisition.

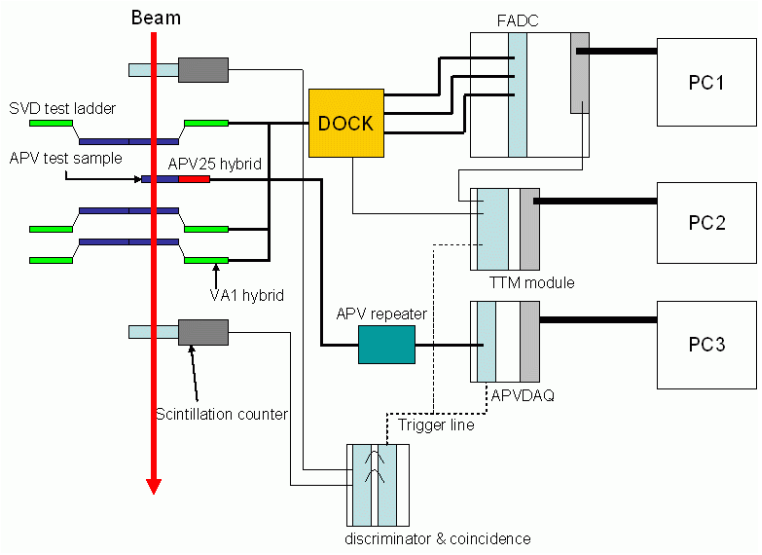

Figure 5.4: A Schematic diagram of readout system at the beam test

5.2 Analysis procedure

The data used for the analysis were taken with 50ns peaking time, 12 sample multi-peak mode, and -80V bias voltage. The analysis procedure is as follow.

1. A data sparsicication and clustering to find the hit position
2. Reconstruction of the proper track by using the hit position
3. Calculation of the deviation of residual on the prototype-sensor

After all, we can obtain the spatial resolution and hit-finding efficiency.

5.2.1 Data sparcification

First, I mention the raw data. As concerns the raw data read by VA1TA readout, the trigger timing was adjusted so that the data becomes shaping. On the other hand, one read by AVP25 readout, 12 sample data are taken with an interval of 25ns in one event. At this run, we fixed to use the 4th sample data as the raw data.

As shown in Equation(5.1), the raw data (Raw) consists of signal charge yield (S), pedestal (P), and common-mode-shift (CMS). S is composed of signal deriving from particles ($S^{particle}$) and from intrinsic-noise (S^{noise}), and these can't be distinguished. S is obtained after subtracting pedestal and CMS. P and RMS of $S^{particle}$ (N) can be calculated in 600 events of local run (Appendix A).

$$Raw = S + P + CMS \tag{5.1}$$

During the performance, we calculated CMS at each event. When signal-to-noise ratio on a strip is larger than 3 (S/N>3), we define it as a "hit strip". In calculation of CMS we removed all hit strips, then we can consider that S of remaining strips doesn't include $S^{particle}$ as same as the local run.

We define S^{noise} as vanishing by summing up over all hit strips (as same as Appendix A Equation A.1). CMS at a certain event is obtained by averaging pedestal-subtracted ADC counts,

$$CMS = \frac{\sum_h (Raw_h - P_h)}{[Number\ of\ hit\ strips]} \tag{5.2}$$

where Raw_h, P_h is raw data and signal charge yield at h-th hit strip.

5.2.2 Clustering

To find a hit signal and its hit position, first we define a cluster. When a charged particle goes through the sensor, the hit signal consists of two or more adjoined strips. This is called a cluster. We reconstruct clusters based on the observed signal charge yield(S).

1. Search for a "cluster seed" strip, whose S/N is larger than the cluster-seed-threshold(C_{seed}) and S is largest in all strips.

2. Define "cluster tail" strips, if the S/N of the neighboring strips of the cluster seed strip is larger than the cluster-tail-threshould (C_{tail}).

3. Without selected strips, repeat 1∼2 procedure while cluster seed can be found.

Moreover we select clusters whose cluster signal to noise ratio($S_{cluster}/N_{cluster}$) is larger than $C_{cluster}$ as follows,

$$S_{cluster}/N_{cluster} = \frac{\sum_i S_i}{\sqrt{\sum_i {N_i}^2}}, \tag{5.3}$$

In this analysis, C_{seed}, C_{strip}, and C_{clust} is set to 5.0, 3.0, and 10.0, respectively.

The cluster reconstruction of VA1TA data is also performed with the same manner. We combine the APV25 and VA1TA data based on the event tag

information. Then, we select an event that has cluster signals in the all four layers.

The beam hit position is calculated using the center of gravity method using the cluster. Because the SSD is used, only the one dimension position information can be obtained.

5.2.3 Reconstruction of track

To obtain a proper track, we used three DSSDs with VA1TA system for telescope. The alignment of these DSSDs are well-corrected (Appendix C).

First, to find proper hit positions on each DSSD, we apply the cluster width cut. Cluster width is the number of cluster seed and cluster tail strips. Figure5.5, Figure5.6 shows the Cluster width distribution of the three DSSDs for each direction.

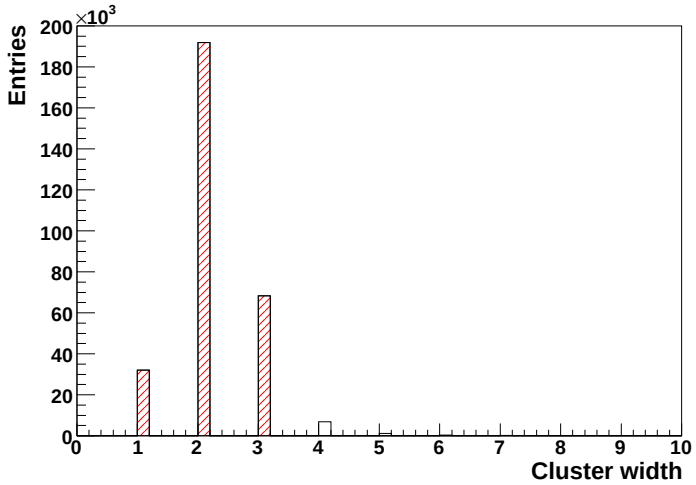

Figure 5.5: Cluster width distribution on three DSSDs for vertical coordinates

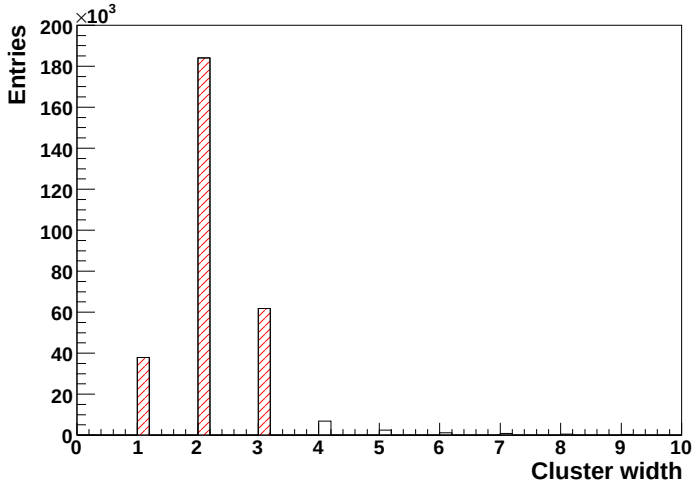

Figure 5.6: Cluster width distribution on three DSSDs for horizontal coordinates

The π^- beam is injected so perpendicularly that cluster width of most of clusters is 1$\sim$3. I selected clusters whose width is less than 4 (red-slashed portion).

However, since there are one or more such selected positions on each DSSDs for each direction, what we have obtained is the candidate of proper hit positions. To reconstruct a proper set of such positions, first we fit linear tracks for all possible sets of hit position. Next we select the track and the set of position whose χ^2 is minimum, where we assume that three DSSDs have the same intrinsic-spatial-resolution. For example as Figure5.7, there are 2-1-2 hit positions(point X) in the three DSSD system. We can fit 4 possible tracks(black-dotted and red arrows). Red one has minimum χ^2, then we select the track and concerning positions.

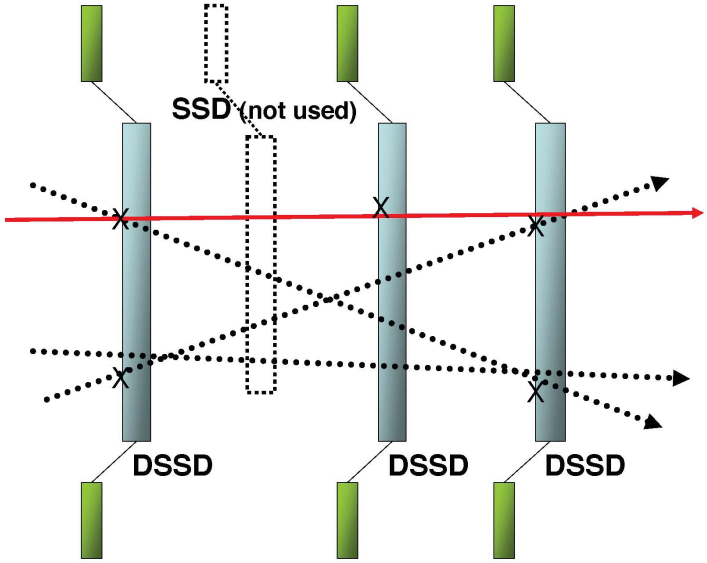

Figure 5.7: A diagram of example of tracking

Figure5.8 shows χ^2 distribution between the selected three hit positions and track. We select a track whose χ^2 is less than 3 (red-slashed portion). This cut save about 75% of data in which at least we can fit one track.

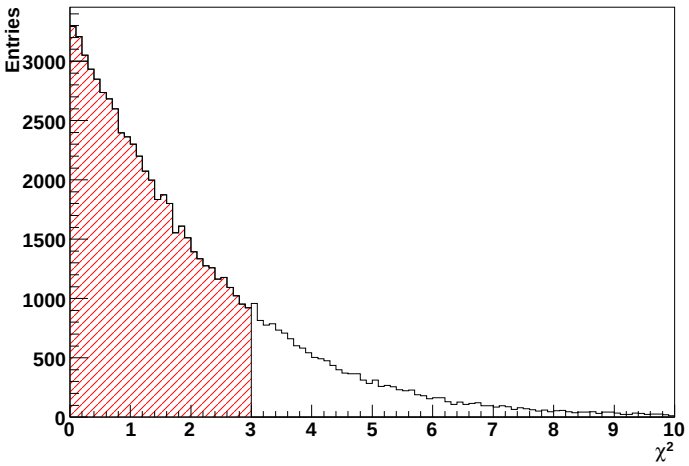

Figure 5.8: χ^2 distribution of the track

5.2.4 Calculation of the sigma of residual

In this section, I will calculate the sigma of residual ($\sigma_{residual}$) on test sensor with APV25 readout. Residual is represented by this formula.

$$[\text{Residual}] = [\text{Hit position}] - [\text{Track-estimated position}]$$

Similar to three DSSDs, there may be one or more hits in a region of the test sensor. For calculation of the residual, we select one which is nearest to the estimated position by the proper track (described in Section5.2.3).

Then, we can plot the residual distribution in each region of test sensor as shown in Figure5.9∼5.13. $\sigma_{residual}$ is obtained by the gaussian fit as shown in Table5.2.4.

We define the *Proper-hit* on the test sensor which is in $3\sigma_{residual}$ search window (Equation5.4).

$$Proper\ hit: \quad |\ [Residual]\ | < 3\sigma_{residual} \tag{5.4}$$

Type	S75-2	S75-3	S75-4	S100-3	S100-5
$\sigma_{residual}$ [μm]	19.4	17.5	12.3	24.5	11.9

Table 5.1: Table of $\sigma_{residual}$

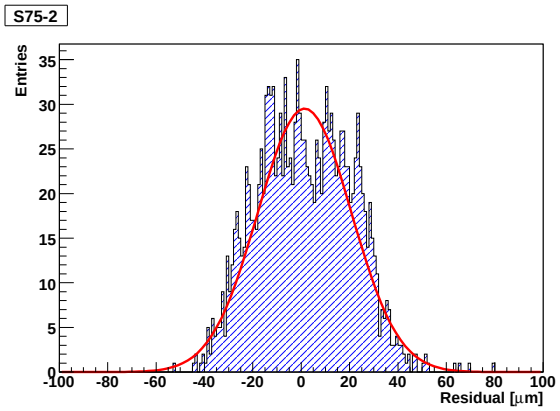

Figure 5.9: Residual distribution(S75-2)

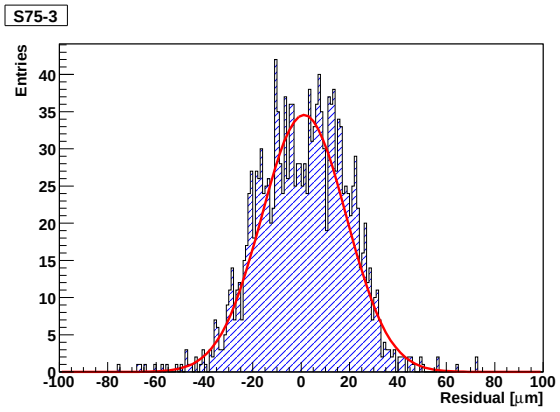

Figure 5.10: Residual distribution(S75-3)

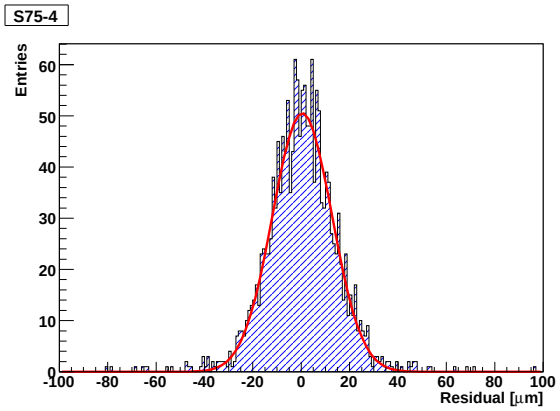

Figure 5.11: Residual distribution(S75-4)

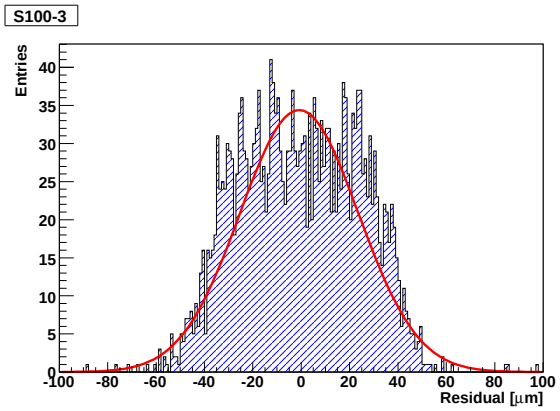

Figure 5.12: Residual distribution(S100-3)

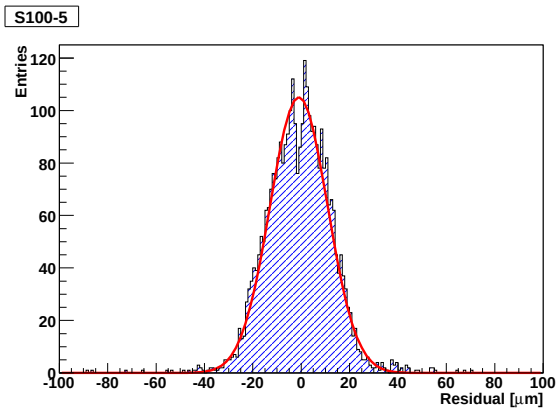

Figure 5.13: Residual distribution(S100-5)

5.3 Experiment result

5.3.1 Hit-finding efficiency

We define the denominator and numerator of hit-finding efficiency as follows.

- The denominator: Number of hits which pass thorough acceptance region
- The numerator: Number of hits in the $3\sigma_{residual}$ search window

  (Number of *Proper-hits* described in Section5.2.4)

Figure5.14 shows the definition of the acceptance region and search window. The acceptance region is the region where the strips connected to readout actually exists. The $3\sigma_{residual}$ search window is represented as follows.

$$|[Hit\ position] - [Estimated\ position\ by\ track]| < 3\sigma_{residual} \tag{5.5}$$

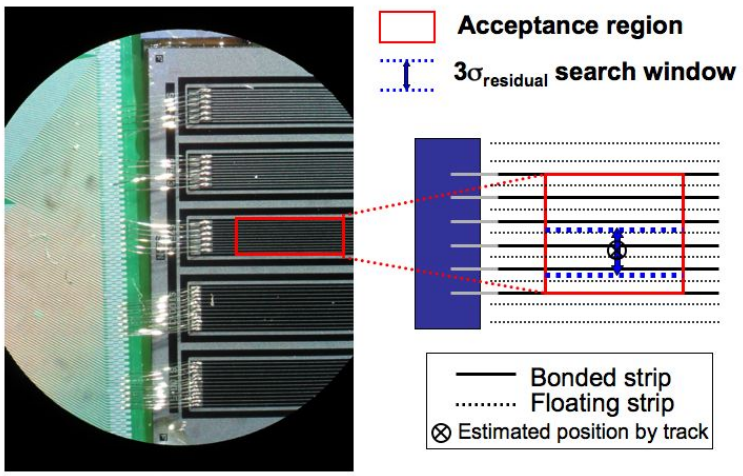

Figure 5.14: A diagram of the region definition for hit-finding efficiency

Table5.2 shows the hit-finding efficiency for each region. For all regions, hit-finding efficiency is good enough (∼99%).

Type	Entries	Hit-finding efficiency(%)
S75-2	1240/1245	99.6±0.2%
S75-3	1333/1349	98.8±0.3%
S75-4	1349/1371	98.4±0.3%
S100-3	1891/1902	99.4±0.2%
S100-5	2662/2699	98.6±0.2%

Table 5.2: Hit-finding efficiency of the test sensor

5.3.2 Signal to noise ratio

We define signal to noise ratio (S/N). S is the charge from a MIP particle and is obtained as the peak value of cluster energy distribution of *Proper-hits*(Section5.2.4) as shown in Figure5.15∼5.19. N is the noise averaged in each region.

The energy loss of a charged particle in material follows the Landau distribution. However the electric noise is always superimposed to the hit signals, and it follows the Gaussian distribution. Then, the convolution of Landau and Gaussian functions are applied to fit the distribution (red-line). By this fit, we can obtain the peak value. The noise of each strip is calculated in the 600 events of local run for APV25 (Appendix A), and averaged by number of strips in each region.

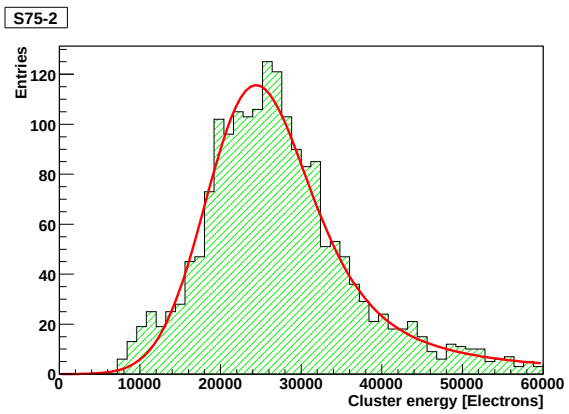

Figure 5.15: Cluster energy distribution (S75-2)

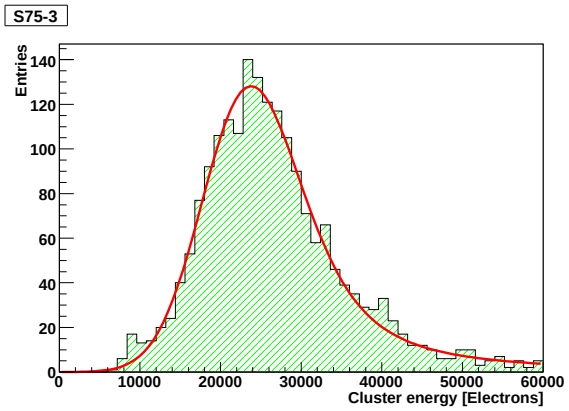

Figure 5.16: Cluster energy distribution (S75-3)

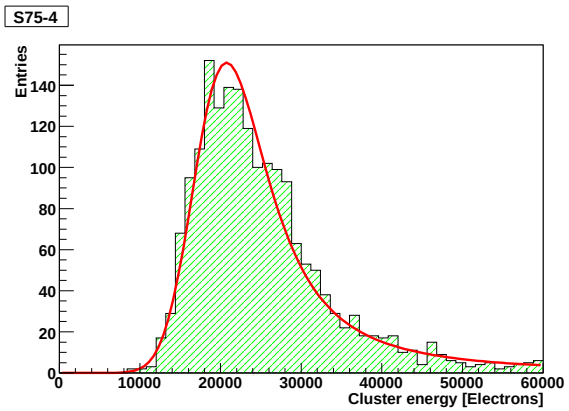

Figure 5.17: Cluster energy distribution (S75-4)

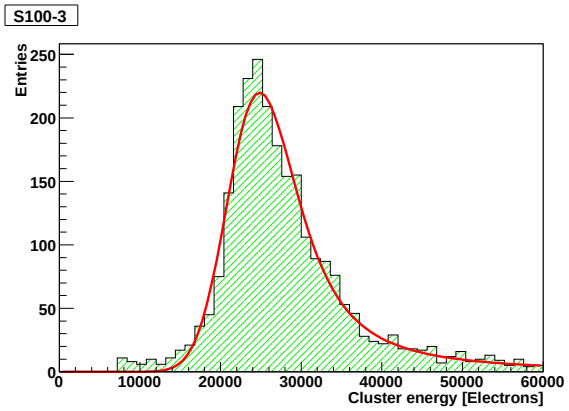

Figure 5.18: Cluster energy distribution (S100-3)

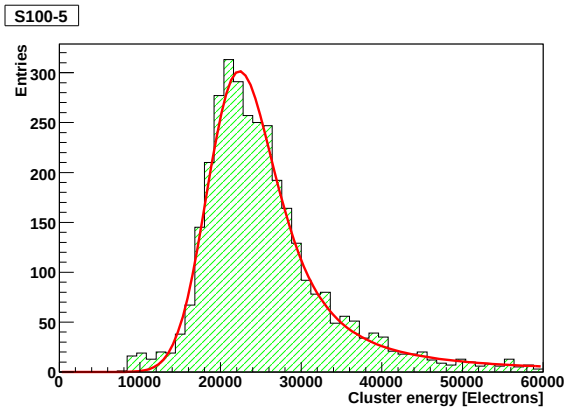

Figure 5.19: Cluster energy distribution (S100-5)

Table5.3 shows the peak value of the cluster energy distribution, noise, and S/N value, where ENC is Equivalent Noise Charge. S/N is required to be more than 20 for the belle experiment, and that is satisfied at all configurations.

Type	S75-2	S75-3	S75-4	S100-3	S100-5
Cluster energy [Electrons]	24402	23788	20739	24846	22345
Noise [ENC]	719	674	657	826	856
S/N	33.9	35.3	31.6	30.1	26.1

Table 5.3: Table of Spatial resolution of the test sensor

5.3.3 Spatial resolution

We can estimate the spatial resolution by Equation(5.6),

$$[Spatial\ resolution] = \sqrt{\sigma^2_{residual} + \sigma^2_{tracking} + \sigma^2_{multi}} \tag{5.6}$$

where $\sigma_{tracking}$ is the uncertainty of estimated position, and σ_{multi} is the multiple scattering contribution to the spatial resolution. $\sigma_{tracking}$ is calculated in Appendix C, and it is 6.3 μm. σ_{multi} is estimated at 1.3 μm by a GEANT4 simulation. $\sigma_{residual}$ is estimated in Section5.2.4, then we can calculate the spatial resolution of test sensor with APV25 readout as shown in Table5.4.

Type	S75-2	S75-3	S75-4	S100-3	S100-5
Spatial resolution [μm]	18.2±0.4	16.2±0.4	10.4±0.3	23.6±0.4	10.0±0.2

Table 5.4: Table of Spatial resolution of the test sensor

5.3.4 Charge sharing

To understand how the charge from particles in the sensor is shared by one or more sensors, I will show the correlation of the sensors and how many strips counts the signal in a event.

The mean of cluster width is shown in Table5.5. The large mean value of cluster width suggest that the charge deposited in the sensor is well-shared by two or more strips.

	S75-2	S75-3	S75-4	S100-3	S100-5
P-stop gap [μm]	7	15	37	6	56
Mean of cluster width	1.49	1.52	1.68	1.23	1.63

Table 5.5: The mean of cluster width

In Figure5.20∼5.29, the left hand shows the cluster width distribution of hits. The right hand shows the correlations of measured position and the estimated position by the telescope in each region of the test sensor: the vertical axis is the measured position, and the horizontal axis is the estimated position by the telescope. *Red*, *Green*, *Blue* plots are corresponding to hits with cluster width 1, 2, 3 respectively. Positions in both axis are divided by readout pitch and the remainder are plotted, that is, in plots of 75μm pitch sensors, the readout strips are located at 0 and 150μm (floating strips are at 75μm), and in plots of 100μm pitch sensors, the readout strips are located at 0 and 100μm.

The slope becomes gradual around strip-existing position in all plots. How-

ever, there is a notable thing. The sensor with wide P-stop gap behaves as if it has a floating strip. For example, S100-5 has no floating strips, but the slope is gradual around the middle of readout strips.

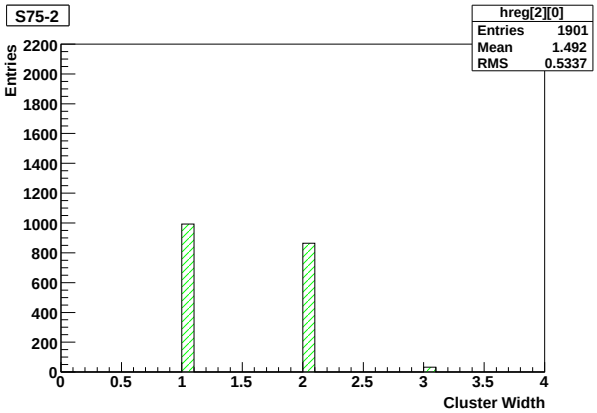

Figure 5.20: Cluster width distribution of hits (S75-2)

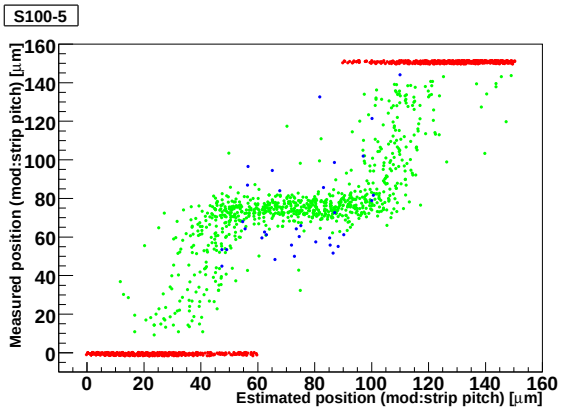

Figure 5.21: The correlation of the measured and estimated position (S75-2)

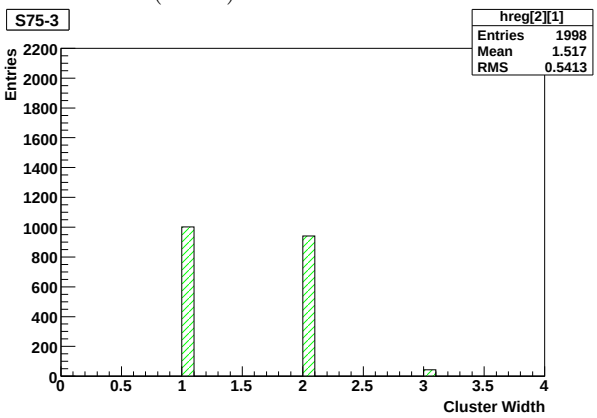

Figure 5.22: Cluster width distribution of hits (S75-3)

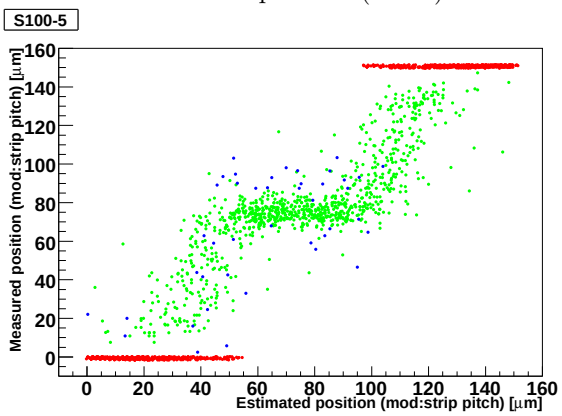

Figure 5.23: The correlation of the measured and estimated position (S75-3)

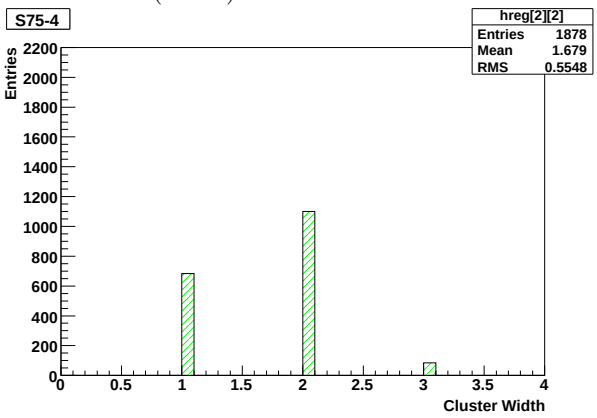

Figure 5.24: Cluster width distribution of hits (S75-4)

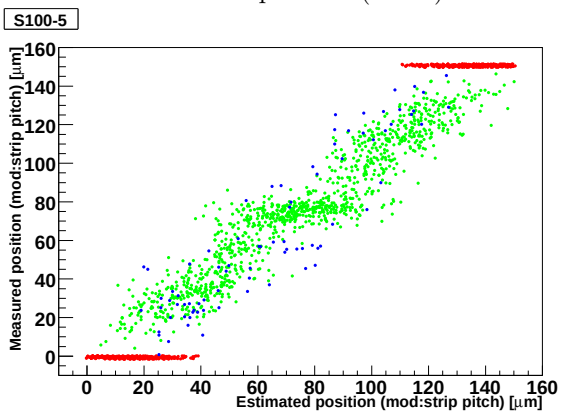

Figure 5.25: The correlation of the measured and estimated position (S75-4)

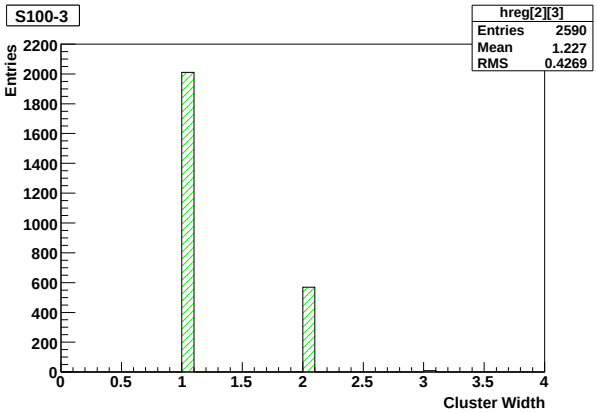

Figure 5.26: Cluster width distribution of hits (S100-3)

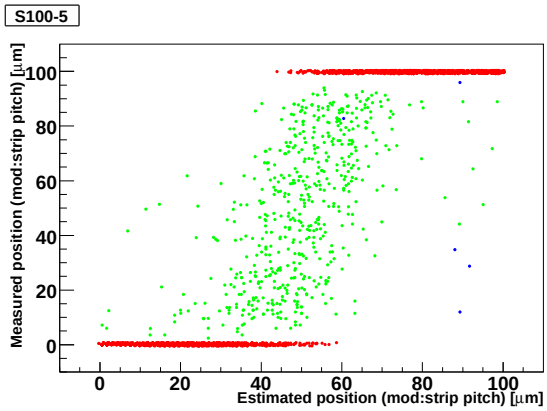

Figure 5.27: The correlation of the measured and estimated position (S100-3)

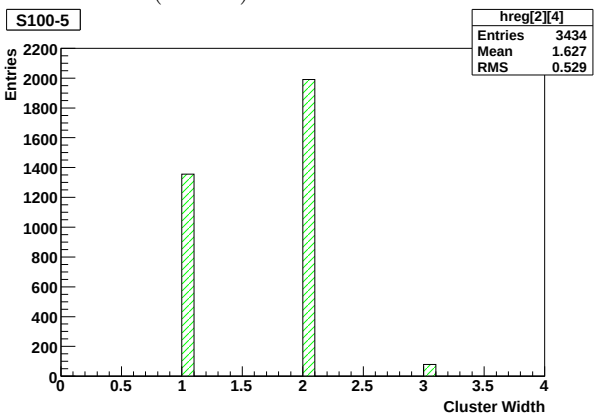

Figure 5.28: Cluster width distribution of hits (S100-5)

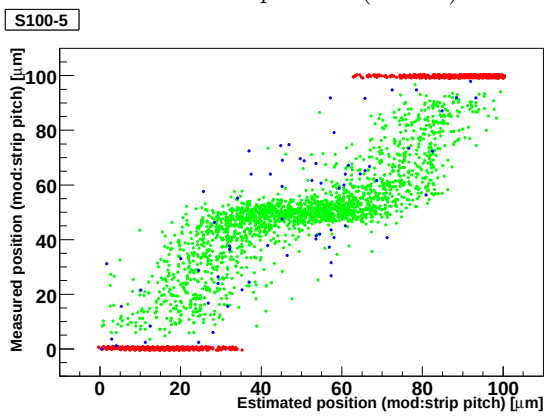

Figure 5.29: The correlation of the measured and estimated position (S100-5)

5.3.5 Results and discussions

Table5.6 shows all the analysis results.

	S75-2	S75-3	S75-4	S100-3	S100-5
Strip pitch [μm]	75	75	75	100	100
(Readout pitch) [μm]	(150)	(150)	(150)	(100)	(100)
N-strip width [μm]	32	24	12	12	12
P-stop width [μm]	12	12	7	35	10
P-stop gap [μm]	7	15	37	6	56
Interstrip capacitance [pF] (at -80V bias voltage)	2.1	1.9	1.6	1.2	1.4
Hit-finding efficiency [%]	99.6±0.2	98.8±0.3	98.4±0.3	99.4±0.2	98.6±0.2
Cluster energy [Electrons]	24402	23788	20739	24846	22345
Noise [ENC]	719	674	657	826	856
S/N	33.9	35.3	31.6	30.1	26.1
Mean value of cluster width	1.49	1.52	1.68	1.23	1.63
Spatial resolution [μm]	18.2±0.4	16.2±0.4	10.4±0.3	23.6±0.4	10.0±0.2
Spatial resolution per strip pitch	0.24	0.22	0.14	0.24	0.10

Table 5.6: All the analysis results

We did a beam test to evaluate the performance of a prototype N-side SSD with APV25 readout. For all configurations, we confirmed the good hit-finding efficiency ($\sim$99%), and enough S/N of the sensor (required to be more than 20).

S100-3 and S100-5, which are different only in the P-stop structure, have almost same detector capacitance, but the spatial resolution is quite different. I plot the spatial resolution as a function of the mean value of cluster width as shown in Figure5.30. The better resolution is due to the larger mean value. We can consider that when the charge from particle is well-shared by multiple strips, the spatial resolution becomes good. Moreover in the region with good resolution like S100-5, the sensor behaves as if it has a floating strip in the middle of two strips where actually there are no strip (Section5.3.4). This effect seems to enhance the ability of charge sharing.

To confirm what cause the well charge sharing, I plot the mean value of

cluster width as a function of P-stop gap (Figure5.31). The larger mean value of cluster width is due to the wider P-stop gap. Thus, the better spatial resolution is due to the wider P-stop gap as shown in Figure5.32.

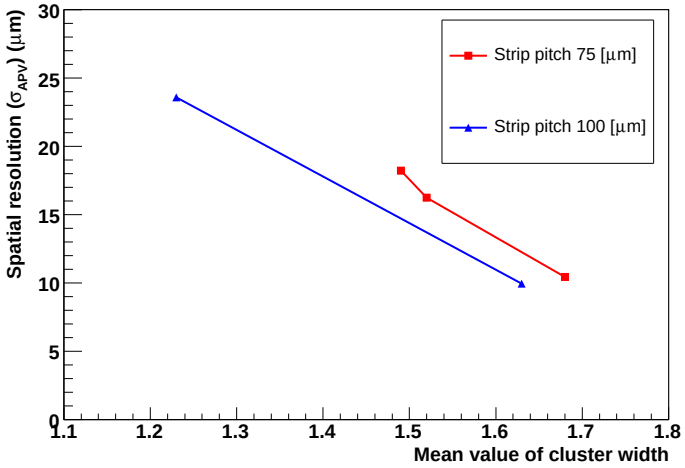

Figure 5.30: The spatial resolution vs Mean value of cluster width

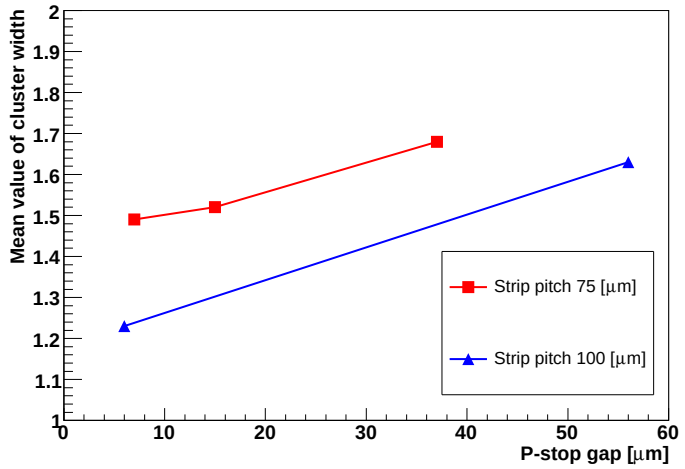

Figure 5.31: The P-stop gap dependence of mean value of cluster width

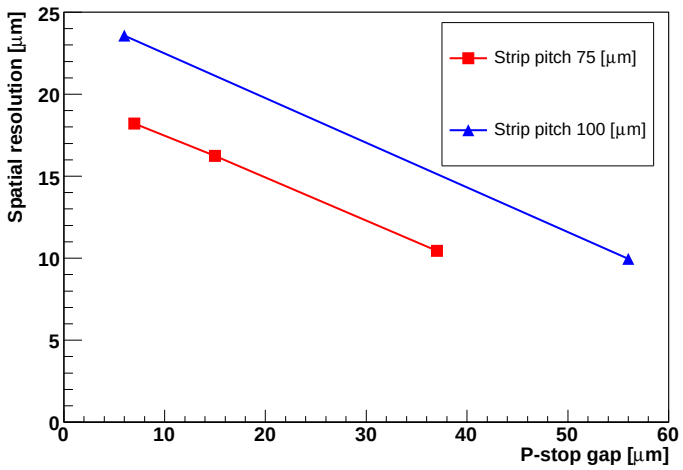

Figure 5.32: P-stop gap dependence of the spatial resolution

Chapter 6

Summary and Conclusion

The employment of APV25 readout chip for SVD readout causes increase of the noise from detector capacitance. Then we have to design new DSSD, and we prepare the prototype of the sensor with 5 configurations.

The purpose of this thesis is to evaluate and study the performance of new-designed sensor with APV25 readout. First we measured the capacitance between neighboring strips since it is dominant component of detector capacitance. At the -80V bias voltage which is high enough for the semiconductor to be full-depleted, the measured capacitance is almost same as that of LEP-SI model (Appendix B) which suggests that the sensor with smaller ratio of the strip width to the strip pitch has smaller capacitance.

To measure the performance of the prototype on the close condition to the real operation, we did a beam test by using 4GeV π^- beam. For all configurations, we confirm the good hit-finding efficiency ($\sim$99%), and enough S/N of the sensor (required to be more than 20). About the spatial resolution of the sensor, I find the sensor with wider P-stop gap has better resolution. When P-stop gap is wide, the mean value of cluster width becomes large because the charge from particles passing between two strips are well-shared to both strips,

and this results in the good spatial resolution.

However we have not understood why wider P-stop gap causes the well charge sharing, and the solution of this question is one of the future studies for the silicon strip sensor. As another future task, we have to study the influence of the radiation damage. The radiation dose of the SVD is expected to increase, and especially the leakage current of the sensor increases by γ-ray irradiation, which causes the larger shot noise. Thus, we need to evaluate its radiation hardness by irradiating γ-rays to the sensor.

Appendix A

Local run

DAQ system of APV25 readout takes first 600 events for pedestal and noise evaluation by the internal random trigger.

We define,

$$\sum_{eve=1}^{600} S^{noise}(eve, ch) = 0, \sum_{ch=1}^{128} S^{noise}(eve, ch) = 0 \tag{A.1}$$

where S^{noise}(eve,ch) is the signal witch derives from intrinsic noise depending on the event and channel. And define,

$$\sum_{eve=1}^{600} CMS(eve, ch) = 0 \tag{A.2}$$

where CMS(eve) is common-mode-shift which depend on the event. CMS is the external noise which influences the entire chip, and whose ADC counts change with the same amount for all channels.

In this run, we can consider that there are no signals deriving from particles. Then, the ADC counts of the local run is shown as follows,

$$ADC(eve, ch) = S^{noise}(eve, ch) + P(ch) + CMS(eve) \tag{A.3}$$

where P(ch) is pedestal. The pedestal is an offset ADC value of each channel.

Then, we can calculate the pedestal,

$$P(ch) = \frac{1}{600} \sum_{eve=1}^{600} ADC(eve, ch) \tag{A.4}$$

CMS of the local run,

$$CMS(eve) = \frac{1}{128} \sum_{ch=1}^{128} [ADC(eve, ch) - P(ch)] \tag{A.5}$$

and S^{noise},

$$S^{noise}(eve, ch) = ADC(eve, ch) - P(ch) - CMS(eve) \tag{A.6}$$

The intrinsic noise at each channel (N(ch)) is calculated as the RMS of S^{noise}.

$$N(ch) = \sqrt{\frac{1}{600} \sum_{eve=1}^{600} ({S^{noise}}^2)} \tag{A.7}$$

Appendix B

LEP-SI model

LEP-SI model is used for the estimation of the detector capacitance. the details of this model is describe in [3] and [7].

A DSSD has a finite number of strips with a certain width placed regularly. In this model, the interstrip capacitance C_i is a function of the ratio of strip width W to strip pitch p.

$$C_i = \begin{cases} \frac{\epsilon}{\pi} \ln(2\frac{1+\sqrt{k}}{1-\sqrt{k}})L & 0 \leq k \leq 0.7 \\ \frac{\epsilon\pi}{\ln(2\frac{1+\sqrt{k'}}{1-\sqrt{k'}})}L & 0.7 \leq k \leq 1.0 \end{cases} \tag{B.1}$$

where $k = W/p$, $k' = \sqrt{1-k^2}$, ϵ is the dielectric constant of silicon, and L is the strip length. FigureB.1 shows the calculated capacitance as a function of k with $L = 30mm$.

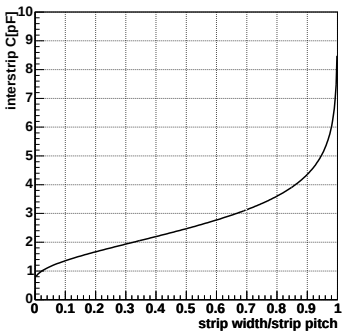

Figure B.1: The plot of interstrip capacitance at LEP-SI model

Appendix C

Alignment and the spatial resolution of current DSSDs

We put three DSSDs carefully, but they may not precisely line up. Then we have to correct the coordinates of them. Here we define the upstream one as DSSD1, the middle one as DSSD2, and the downstream one as DSSD3.

There are two assumption.

1. All three DSSDs have the same spatial resolution.

2. DSSD1 and DSSD3 are perfectly aligned.

   (Even if DSSD1 and 3 are actually not well-aligned, we can't distinguish whether they are not well-aligned or the beam incidence is not perpendicular.)

Then we correct the coordinates of DSSD2. FigureC.1 is the diagram of alignment. First, we connect the hit of DSSD1 and that of DSSD3 with a line. If DSSD2 is perfectly aligned, the hit of DSSD2 comes just on the line. We plot the difference between the hit of DSSD2 and the line, and obtain the sigma of the distribution (σ_{diff}). We rotate DSSD2 on the plane vertical to the beam

line so that σ_{diff} is minimized. The rotation angle dependence of σ_{diff} is shown in FigureC.2, and the difference distribution at the minimizing rotation angle is shown in FigureC.3. We can apply the parallel-shift to DSSD2 by using the mean of this distribution.

Now we have optimized the rotation and parallel-shift for DSSD2. Repeating this procedure by changing the DSSD2 position in the beam direction (define Z-direction), we can optimize the Z-position which minimize σ_{diff}.

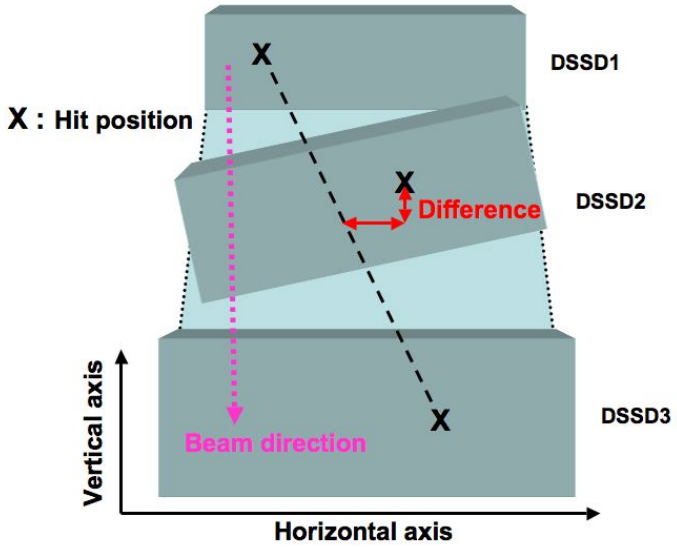

Figure C.1: Diagram of alignment

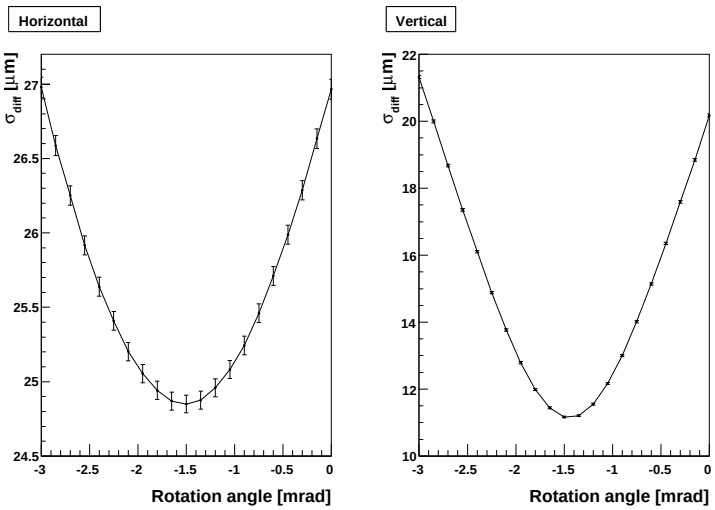

Figure C.2: The rotation angle dependence of σ_{diff}

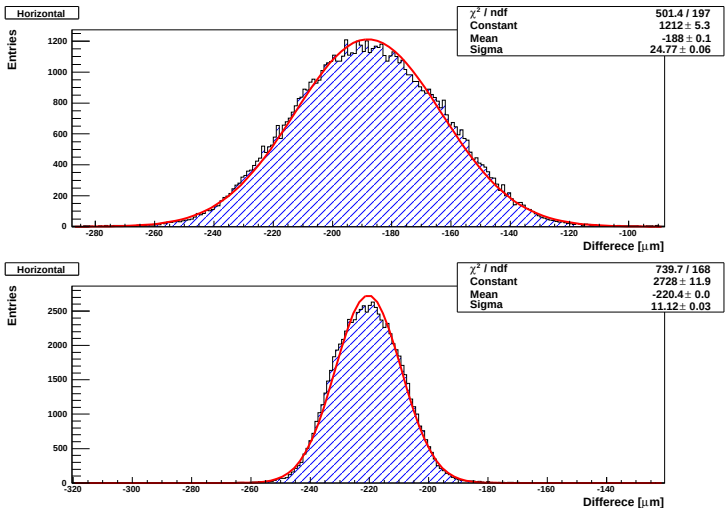

Figure C.3: The difference distribution at the minimizing rotation angle

The spatial resolution of the DSSDs (σ_{DSSD}) is obtained by the σ_{diff}. Define the hit position on DSSD1, 2, 3 as X_1, X_2, X_3, and the Z-position of them as $Z_1 \equiv 0$, $Z_2 = 17mm$, $Z_3 = 40mm$, then the difference is represented by the X_2 and estimated position by the line (X_L),

$$[\text{Difference}] = X_2 - X_L$$

then,

$$\sigma_{diff} = \sqrt{\sigma_{DSSD}^2 + \sigma_{Line}^2} \tag{C.1}$$

where σ_{Line} is the uncertainty of X_L which is,

$$X_L = \frac{(Z_3 - Z_2)X_1 + Z_2 X_3}{Z_3} \tag{C.2}$$

then,

$$\sigma_{Line} = \frac{\sqrt{(Z_3 - Z_2)^2 + Z_2^2}}{Z_3}\sigma_{DSSD} \tag{C.3}$$

where Z_3 are pre-known constant and Z_2 is earlier optimized one. Then we can calculate σ_{DSSD} by EquationC.1, C.3 and the difference distribution as shown in TableC, where P-side read the horizontal coordinate, and N-side is to the vertical coordinate.

Type	P-side	N-side
σ_{DSSD} [μm]	20.2±0.09	9.1±0.04

Table C.1: Table of σ_{DSSD}

As same as this calculation, we can calculate the uncertainty of track (σ_{Track}) described in Section5.2.3. The track parameter A, B ($X = AZ + B$) is found as follows.

$$A = \frac{3(\sum_{i=1}^{3} Z_i X_i) - (\sum_{i=1}^{3} Z_i)(\sum_{i=1}^{3} X_i)}{3(\sum_{i=1}^{3} Z_i^2) - (\sum_{i=1}^{3} Z_i)^2} \tag{C.4}$$

$$B = \frac{(\sum_{i=1}^{3} Z_i)^2(\sum_{i=1}^{3} X_i) - (\sum_{i=1}^{3} Z_i X_i)(\sum_{i=1}^{3} Z_i)}{3(\sum_{i=1}^{3} Z_i^2) - (\sum_{i=1}^{3} Z_i)^2} \tag{C.5}$$

Define the estimated position by the track, and Z-position of the test sensor as X_{Track}, and Z_a,

$$X_{Track} = AZ_a + B \tag{C.6}$$

Then by using EquationC.4∼C.6 and σ_{DSSD},

$$\sigma_{track} = \sqrt{\frac{\sum_{j=1}^{3}\left[(3Z_j - \sum_{i=1}^{3} Z_i)Z_a + (\sum_{i=1}^{3} {Z_i}^2) - (\sum_{i=1}^{3} Z_i)Z_j\right]^2}{\left[3(\sum_{i=1}^{3} Z_i^2) - (\sum_{i=1}^{3} Z_i)^2\right]^2}} \times \sigma_{DSSD} \tag{C.7}$$

The test sensor only read the vertical coordinate, and finally we obtain σ_{track} by using σ_{DSSD}(N-side).

$$\sigma_{track} = 6.34\ [\mu m] \tag{C.8}$$

Bibliography

[1] M.Friedl (Vienna University of Technology) Doctor Thesis (2001)

[2] M. Friedl, APVDAQ Reference Manual.

[3] R.Abe (Niigata University) Master Thesis (2002)

[4] S.Ono (T.I.T) Master Thesis (2006)

[5] Y.Nakahama (Tokyo University) Master Thesis (2006)

[6] J.Kaneko (T.I.T) IEEE Trans. Nucl.Sci., VOL49,NO.4 (2002),1593

[7] D.Hussun IEEE Trans. Nucl.Sci., VOL41,NO.4 (1994),811

[8] The Belle Collaboration The Belle detector [KEK Progress Report 2000-4]

[9] Y.Fujisawa (Tohoku University) Master Thesis (2002)

[10] H.Yamamoto (Tohoku University) Lecture notes [Quantum Field Theory]

[11] Y.Fujisawa (Tohoku University) Master Thesis (2002)

[12] N.Kikuchi (Tohoku University) Master Thesis (2006)